 doi:10.20944/preprints202106.0484.v1

Article

Shortcut Faults and Lateral Spreading Activated in a Pull-Apart Basin by the 2018 Palu Earthquake, Central Sulawesi, Indonesia

Keitaro Komura* [1] **and Jun Sugimoto** [2]

[1] Central Research Institute of Electric Power Industry, 1646 Abiko, Abiko-shi, Chiba-ken 270-1194, Japan, komukeit@criepi.denken.or.jp
[2] PASCO Corporation, 1-1-2 Higashiyama, Meguro-ku, Tokyo 153-0043, Japan, joutno7374@pasco.co.jp
* Correspondence: komukeit@criepi.denken.or.jp

Abstract: Our understanding of pull-apart basins and their fault systems has been enhanced by analog experiments and simulations. However, there has been no opportunity to compare the faults that constitute pull-apart basins with surface ruptures during earthquakes. In this study, we investigated the effects of a 2018 earthquake (Mw 7.5) on a pull-apart basin in the Palu-Koro fault system, Sulawesi Island, Indonesia, using geomorphic observations in digital elevation models, optical correlation with pre- and post-earthquake satellite images. A comparison of active fault traces determined by geomorphology with the locations of surface ruptures from the 2018 earthquake shows that some of the boundary faults of the basin are inactive and that active faulting has shifted to basin-shortcut faults and relay ramps. We also report evidence of lateral spreading, in which alluvial fan materials moved around the end of the alluvial fan. These phenomena may provide insights for anticipating the location of future surface ruptures in pull-apart basins.

Keywords: 2018 Palu earthquake, pull-apart basin, basin-shortcut fault, lateral spreading, optical correlation

1. Introduction

Pull-apart basins are tensile structures associated with lateral-displacement fault; they form by the development of a group of secondary normal faults oblique to the main lateral-displacement fault [1–8]. The development of pull-apart basins has been explored with analog sandbox models [7–14] and model calculations [15–19]. Wu et al. [8] used sandbox models of pure strike-slip and transtensional basement fault systems to investigate the development of pull-apart basins in both tectonic settings. They reported that en-echelon sidewall faults oblique to the principal displacement zones develop first (Figure 1a), forming a primary pull-apart basin. Eventually, lateral faults form shortcuts that transfer displacement across the basin (Figure 1b), and the basin subsides further upon the formation of relay ramps connecting the sidewall faults (Figure 1c). Next, lateral and vertical displacements separate into distinct domains along the basin's boundaries, enabling smaller internal basins to form and elongating the entire pull-apart basin (Figure 1d). The mature pull-apart basin eventually transitions into a simple lateral fault zone [6, 20]. The Dead Sea Basin of the Dead Sea fault system [3, 21, 22] and the Gulf of California along the San Andreas fault zone [23–26] have been shown to display active fault properties that are consistent with sandbox experiments, and their development has been compared with analog experiments [12]. However, there has been no opportunity to compare coseismic surface ruptures with the faults that constitute a pull-apart basin.

Preprints (www.preprints.org) | NOT PEER-REVIEWED | Posted: 18 June 2021 doi:10.20944/preprints202106.0484.v1

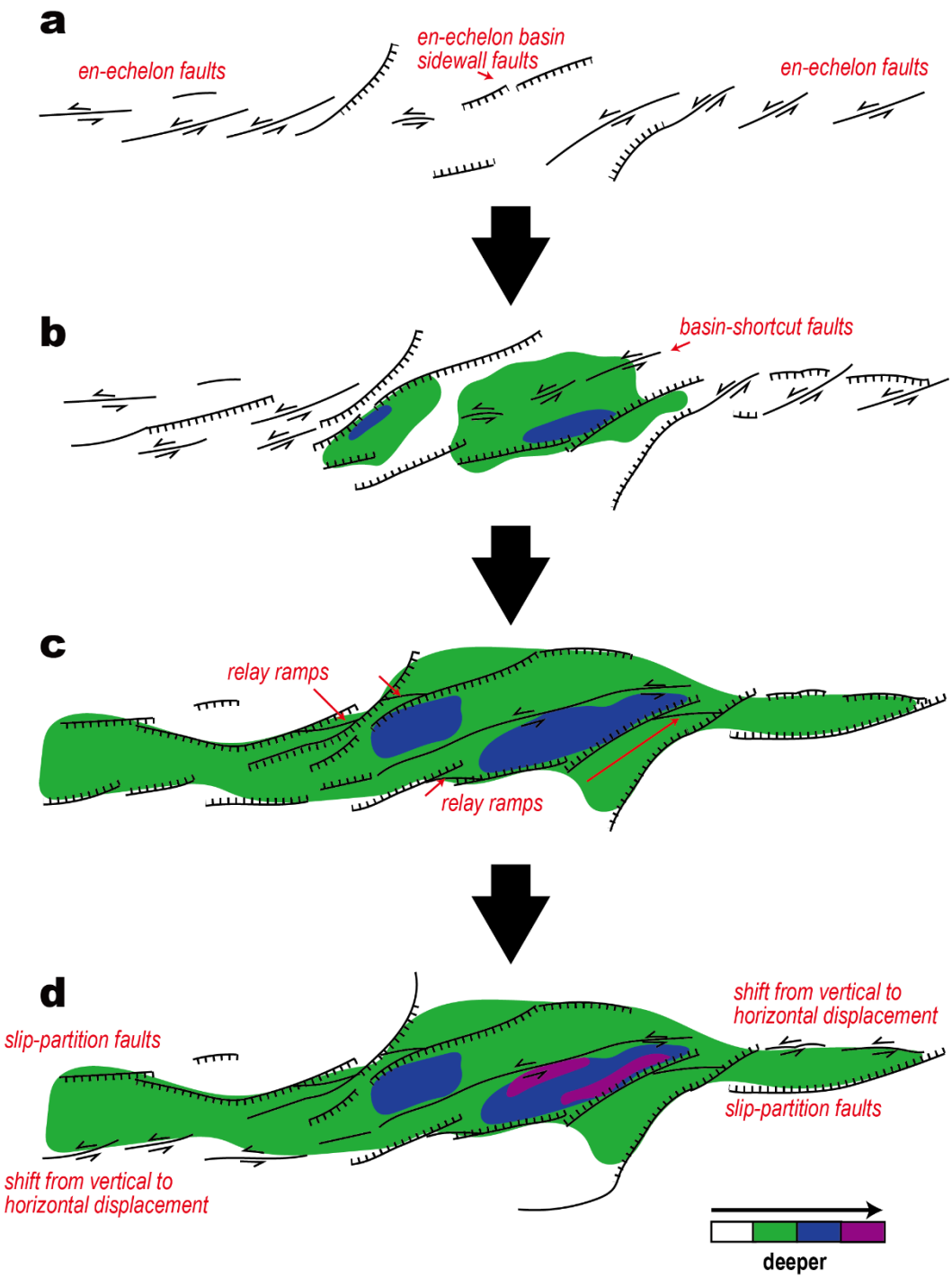

Figure 1. Schematic diagram showing development of a transtensional pull-apart basin, based on sandbox experiments; modified from Wu et al. [8].

In Sulawesi Island, Indonesia, a pull-apart basin is present near the city of Palu along the Palu-Koro fault (Figure 2), which ruptured during the Mw 7.5 earthquake on 28 September 2018 ('the 2018 earthquake' hereafter), causing extensive damage mainly in the Palu basin, the southward structural continuation of Palu Bay, due to tsunami waves and liquefaction landslides [27–29]. The earthquake produced distinct surface ruptures in the Palu basin [30–33], and many studies have used satellite and seismic data to estimate fault models and rupture propagation [34–42]. However, few studies have adequately compared the distribution of active faults, defined on the basis of geomorphic features, with the location of 2018 surface ruptures. Such a study may provide insights that can

Preprints (www.preprints.org) | NOT PEER-REVIEWED | Posted: 18 June 2021 doi:10.20944/preprints202106.0484.v1

improve predictions of where surface ruptures will appear during earthquakes in this and other pull-apart basins.

In this study, we used optical correlation method using Sentinel-2 and SPOT-6 optical satellite imagery to locate the surface ruptures of the 2018 earthquake. We also used digital elevation model (DEM) data to determine the detailed topography of the Palu-Koro fault system and identified active segments of the faults defining the Palu pull-apart basin on the basis of geomorphology ('geomorphically active faults' hereafter). As a result, we found that some of the geomorphically active boundary faults of the Palu basin were inactive and that a newly identified basin-shortcut fault was active during the 2018 earthquake. Furthermore, we found that lateral spreading, which is independent of the direction of fault movement, may have occurred simultaneously within the nearly flat interior of the basin. Because these phenomena are likely during earthquakes in other pull-apart basins in similar tectonic settings, it is necessary to reconsider the interpretation of the associated tectonic geomorphology.

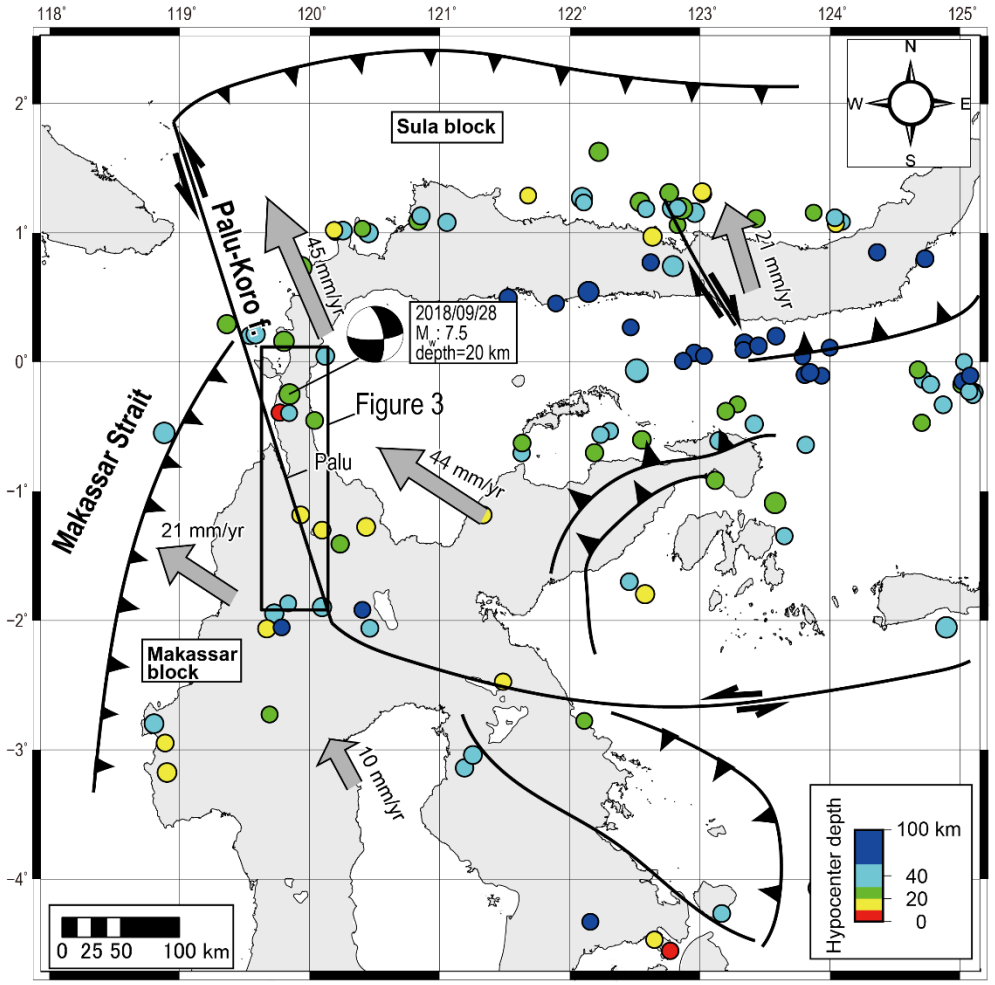

Figure 2. Location map showing topography of Sulawesi island. Major tectonic faults are based on Bellier et al. [43]. Circles are epicenters of earthquakes larger than Mw 6.0 between 1900 and 2020 based on the USGS catalog (https://earthquake.usgs.gov/earthquakes/search/). Gray arrows indicate horizontal plate displacements based on GPS data [44]. Black lines indicate major transcurrent and thrust faults (teeth on upthrown side).

 doi:10.20944/preprints202106.0484.v1

2. The 2018 Palu earthquake

The 28 September 2018 earthquake caused extensive damage mainly within the Palu basin (Figure 3). The earthquake was triggered by the rupture of more than 200 km of the Palu-Koro fault extending from the Tanimbaya Peninsula in the north to near Labua in the south [34–40]. Post-earthquake field surveys mapped a surface rupture 70 km long in the Palu basin [30–33], and surface ruptures on the seafloor of Palu Bay were documented after the earthquake [33]. The earthquake caused left-lateral displacements as great as about 6 m and vertical displacements of about 5 m at the surface [30–33]. Liquefaction-induced landslides within the Palu basin also caused significant damage [27–29].

Sulawesi Island incorporates a complex of several microplates near the triple junction of the Eurasia, Philippine Sea, and Australia plates [43–51]. The Palu-Koro fault is a left-lateral fault between the Sula and Makassar blocks that strikes N20°W and extends about 500 km from beneath the Makassar Strait into the central section of Sulawesi Island (Figure 2). The onshore section of the Palu-Koro fault has been mapped based on satellite images and 30-m DEMs [51–54]. A post-earthquake airborne lidar survey allowed the active fault to be mapped in detail [33]. A geologic slip rate of 35 ± 8 mm/yr was reported for the Palu-Koro fault based on cumulative river offsets within the Palu basin [54]. A geodetic slip velocity of ~40 mm/yr was estimated from GPS surveys since 1992 [44, 55–57]. The paleoseismic record estimated from trenching studies includes at least three events in the past 2000 years for an average recurrence interval of 700 years [52]. Furthermore, paleoseismic trenching conducted in the southern part of the basin after the 2018 earthquake [58] revealed that five earthquakes had occurred since A.D. 1338, including the 2018 earthquake, and estimated a shorter average activity interval of 130 years, suggesting that recent paleoseismic events may have been missed in the trench survey [52] conducted on the Palu Basin's left flank.

3. Methods

Although the Palu-Koro fault has been mapped from satellite imagery and 30-m DEMs, tectonic features may have been missed given the dense tropical vegetation on Sulawesi Island. Even mapping based on the post-earthquake lidar survey [33] does not fully clarify the relationship of active fault traces to terraces, fans, or offset rivers. In this study, we performed an integrated topographic interpretation along the Palu-Koro fault using stereopaired morphometric protection index red relief image maps (MPI-RRIMs) [59] based on DEMNAS, a free DEM in Indonesia with an accuracy of about 8.3 m (Figure 4). Stereopaired MPI-RRIMs simultaneously represent the basic terrain parameters of elevation, slope, and convexity and are effective for extracting small tectonic geomorphic features [59]. We created the stereopairs using ArcGIS software (ESRI), QGIS (QGIS Development Team), and the MPI-RRIMs Calculator software package [59] and applied previously published criteria for terrain extraction [60]. With this method, we extracted fluvial terraces, alluvial fans, landslides, river offsets, wind gaps, and pressure ridges and identified both geomorphically active and presumed fault traces with high reliability.

Preprints (www.preprints.org) | NOT PEER-REVIEWED | Posted: 18 June 2021 doi:10.20944/preprints202106.0484.v1

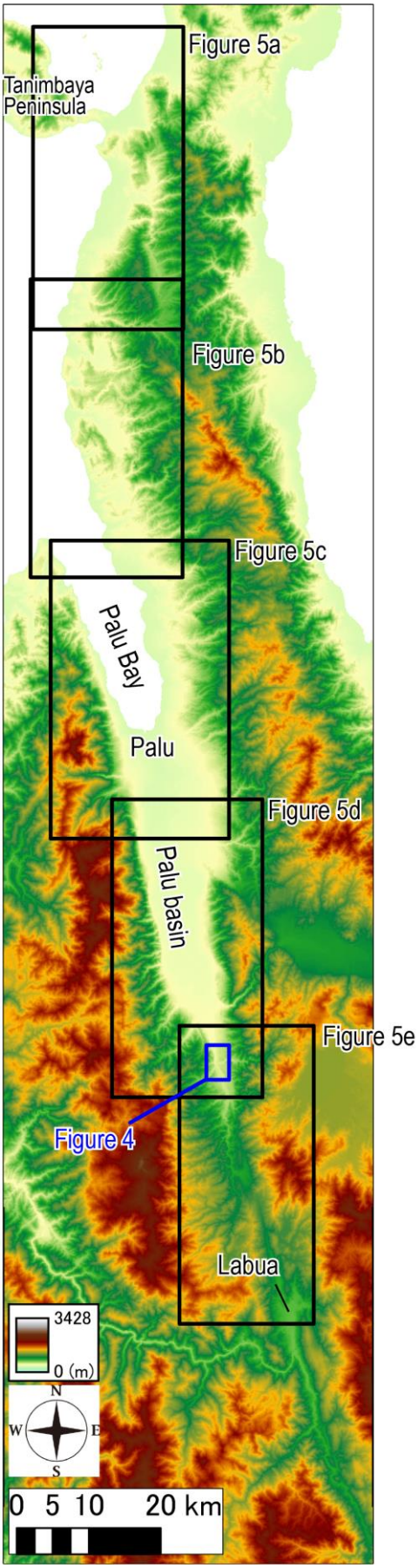

Figure 3. Topographic map of the epicentral region of the 2018 earthquake. The background elevation map is from the ALOS-3D 30-m DEM.

Preprints (www.preprints.org) | NOT PEER-REVIEWED | Posted: 18 June 2021 doi:10.20944/preprints202106.0484.v1

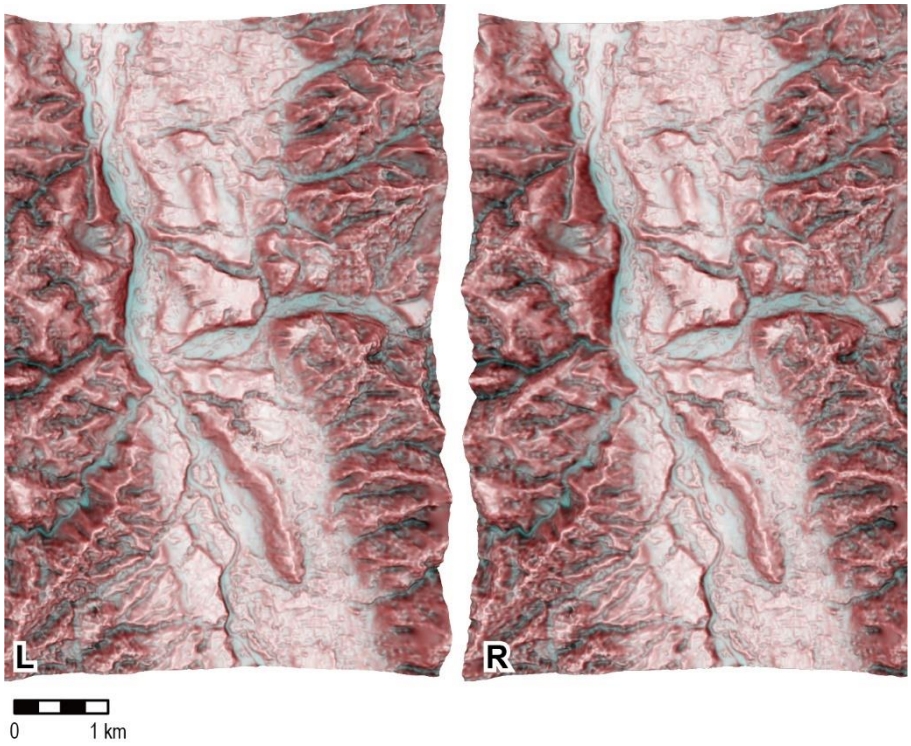

Figure 4. Stereopair of MPI-RRIMs used in this study. See Figure 3 for the location.

To determine the location of the 2018 surface rupture in plan view, we used optical correlation with the Cosi-Corr method [61, 62]. The Cosi-Corr method is used to construct maps of E-W and N-S horizontal displacement based on optical images obtained by satellites and aircraft. It has been used extensively for studies of earthquakes, landslides, and glacier dynamics [63–68] and several studies have used optical correlation to model the faulting of the 2018 earthquake [35, 37, 38, 40, 41]. For this study, we used Sentinel-2 images (orthorectified Level-1C) from before and after the earthquake (Table 1) to create maps of N-S and E-W horizontal displacement for the entire epicentral region. The primary images were taken on 27 September 2018, the day before the earthquake, and on 2 October 2018, four days after the earthquake, to avoid the influence of afterslip. For the Tanimbaya Peninsula (Figure 3), images from 17 September and 22 October 2018 were used to avoid cloud cover. The Cosi-Corr software parameters were as follows: window size, 32 × 32; X and Y step size, 1; robustness iteration, 3 times; and mask threshold, 0.9. A Non-Local Means Filter [69] was applied to the output results, with the H noise parameter set to 2, search area dimension to 21, and patch size to 5 × 5. ENVI software and ENVI classic (both from ESRI) were used for this analysis.

The Level-1c image of Sentinel-2 is orthorectified using band 4 (Red) image, using the previous Sentinel-2 image as a reference image, and obtaining the ground control point by image correlation [70]. The absolute value of the output result may not be correct because the orthorectification was not done by image correlation pre- and post-earthquake. Therefore, when using the Level-1c image, it is possible to determine the location of the discontinuity line that appeared with the earthquake, but it is difficult to determine the exact direction and amount of crustal deformation. So, we additionally conducted an optical correlation using SPOT-6 images (Table 2) to determine the exact direction of crustal deformation (vector field) during an earthquake. The bands used were those of the bundle (P+MS), and the DEM of DEMNAS was used to orthorectify the pre-earthquake images. The post-earthquake images were orthorectified by matching them to the orthorectified pre-earthquake images. The orthorectification process described above was performed using the RPC Orthorectification Workflow and RPC Orthorectification

Preprints (www.preprints.org) | NOT PEER-REVIEWED | Posted: 18 June 2021 doi:10.20944/preprints202106.0484.v1

Using Reference Image of ENVI software. The parameters of Cosi-Corr were as follows: window size, 128 × 32; X and Y step size, 8; and the rest of the parameters were the same as for the Sentinel-2 image. Using the output N-S and E-W displacement maps, a vector field was created using Arc GIS software's model builder function (Data S2 of Supplementary Materials). In particular, the Raster Calculator tool was used to calculate the amount and direction of displacement from both images, and the Focal Statistics tool was used to smooth the vector spacing to the desired output. We created a shapefile containing the displacement values and the direction of displacement (-180 to 180 degrees).

Table 1. Sentinel-2 images used in the optical correlation analysis.

Pair No.	Timing	Date	Pass direction	Resolution	Filename
1	Pre-earthquake	2018/9/27	Descending	10 m	S2B_MSIL1C_20180927T022319_N0206_R103_T50MRD_20180927T055542
	Post-earthquake	2018/10/2	Descending	10 m	S2A_MSIL1C_20181002T022321_N0206_R103_T50MRD_20181002T054141
2	Pre-earthquake	2018/9/27	Descending	10 m	S2B_MSIL1C_20180927T022319_N0206_R103_T50MRE_20180927T055542
	Post-earthquake	2018/10/2	Descending	10 m	S2A_MSIL1C_20181002T022321_N0206_R103_T50MRE_20181002T054141
3	Pre-earthquake	2018/9/17	Descending	10 m	S2B_MSIL1C_20180917T022319_N0206_R103_T50MRE_20180917T054239
	Post-earthquake	2018/10/22	Descending	10 m	S2A_MSIL1C_20181022T022321_N0206_R103_T50MRE_20181022T063218

Table 2. SPOT-6 images used in the optical correlation analysis.

Pair No.	Timing	Date	Resolution	Filename
4	Pre-earthquake	2017/5/16	1.5 m	DS_SPOT6_201705160155554_FR1_FR_1_SV1_E120S01_06499
	Post-earthquake	2018/10/18	1.5 m	DS_SPOT6_201810180156380_JS3_JS3_JS2_JS2_E120S01_02845

4. Results

4.1. Fluvial terraces and fans

Our geomorphic mapping from MPI-RRIM stereopairs shows that fluvial terraces are widely distributed in the study area (Figure 5). We divided the terraces into five levels from high to low (H2, H1, M2, M1, and L1) on the basis of their height with respect to the modern riverbed and their continuity. We also mapped many steeply sloping alluvial fans in the Palu basin. Although it is sometimes difficult to clearly distinguish terraces from alluvial fans, we considered them to be geomorphic surfaces of approximately the same age and classified them as parts of the same surfaces (Figure 6). We did not distinguish between marine and fluvial terraces, although some terraces along the coast were probably more strongly influenced by marine than fluvial forces.

The L1 surface extends from about the same elevation as the modern riverbed to about 10 m above it and includes the largest area of terraces in the study area. Although there is no direct evidence of the terraces' age, they are thought to be abandoned surfaces no older than 7–5 ka, the Holocene sea-level high in the Pacific Rim [71].

The M1 surface is about 30–50 m above the modern riverbed and is widely present in the study area. Bellier et al. [53] reported a ^{10}Be exposure age of 11,000 ± 2300 yr from gravel of a fan on the M1 surface at an elevation of 60 m on the west flank of the Palu basin (Figure 5c). Therefore, the M1 surface is considered a geomorphic surface abandoned by rapid incision during the Younger Dryas [72], immediately after the Last Glacial Maximum.

Preprints (www.preprints.org) | NOT PEER-REVIEWED | Posted: 18 June 2021 doi:10.20944/preprints202106.0484.v1

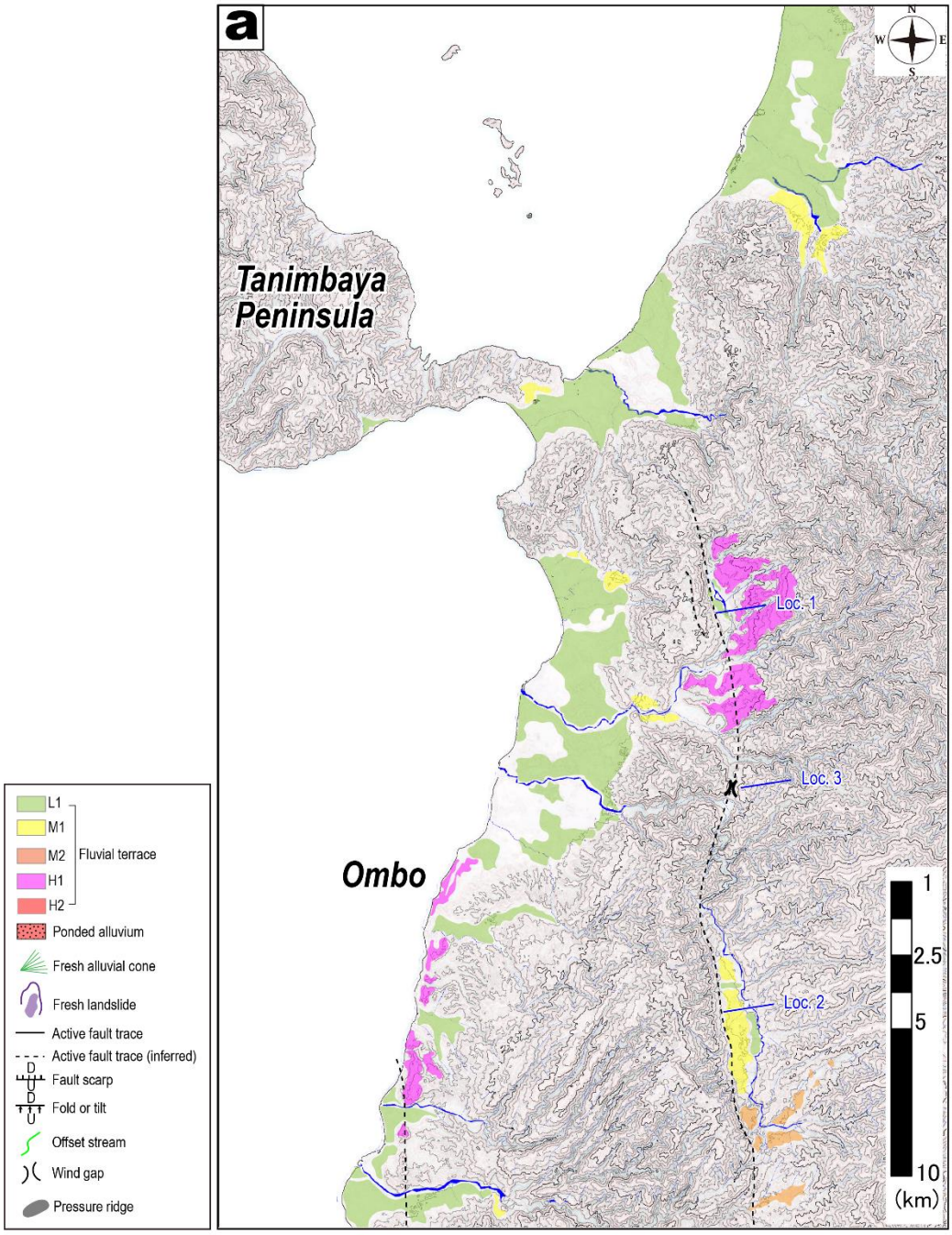

Figure 5. Geomorphic maps along the Palu-Koro fault based on MPI-RRIM stereopairs. See Figure 3 for locations. Base map and contours (10-m interval) were created from DEMNAS. The inset in Figure 5e is an enlarged map of the area near the Saluki River where lateral displacement was measured.

Preprints (www.preprints.org) | NOT PEER-REVIEWED | Posted: 18 June 2021 doi:10.20944/preprints202106.0484.v1

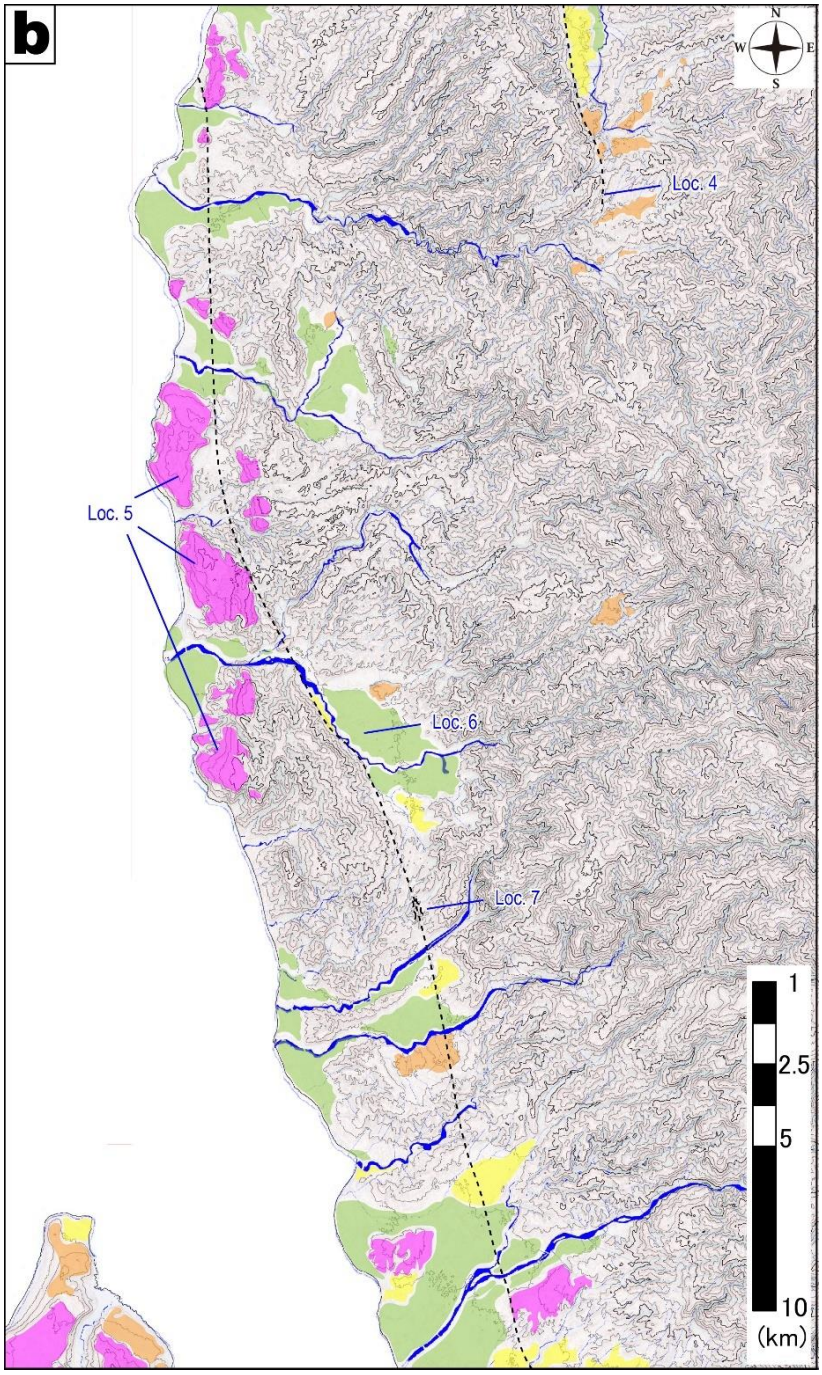

Figure 5. (continued)

Preprints (www.preprints.org) | NOT PEER-REVIEWED | Posted: 18 June 2021 doi:10.20944/preprints202106.0484.v1

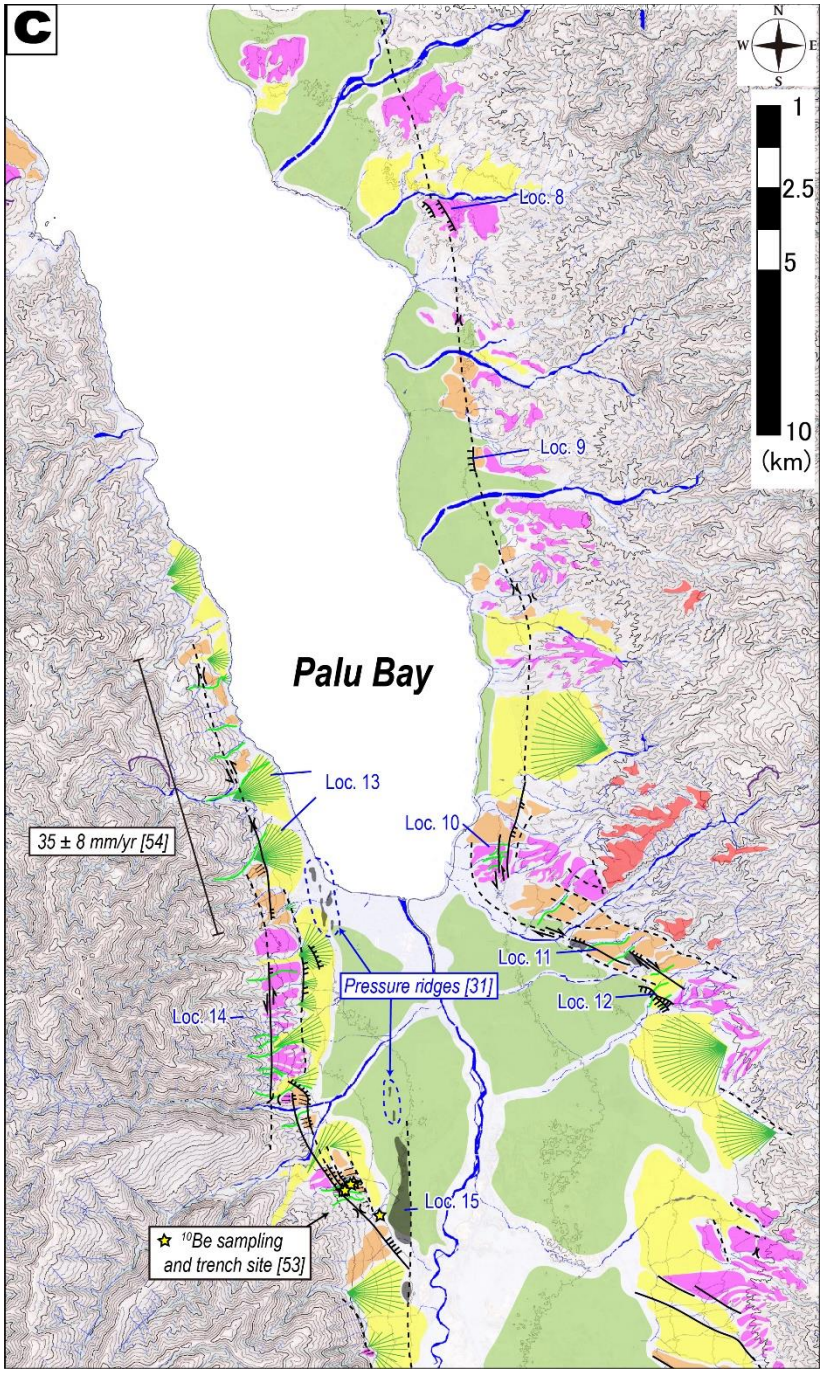

Figure 5. (continued)

Preprints (www.preprints.org) | NOT PEER-REVIEWED | Posted: 18 June 2021 doi:10.20944/preprints202106.0484.v1

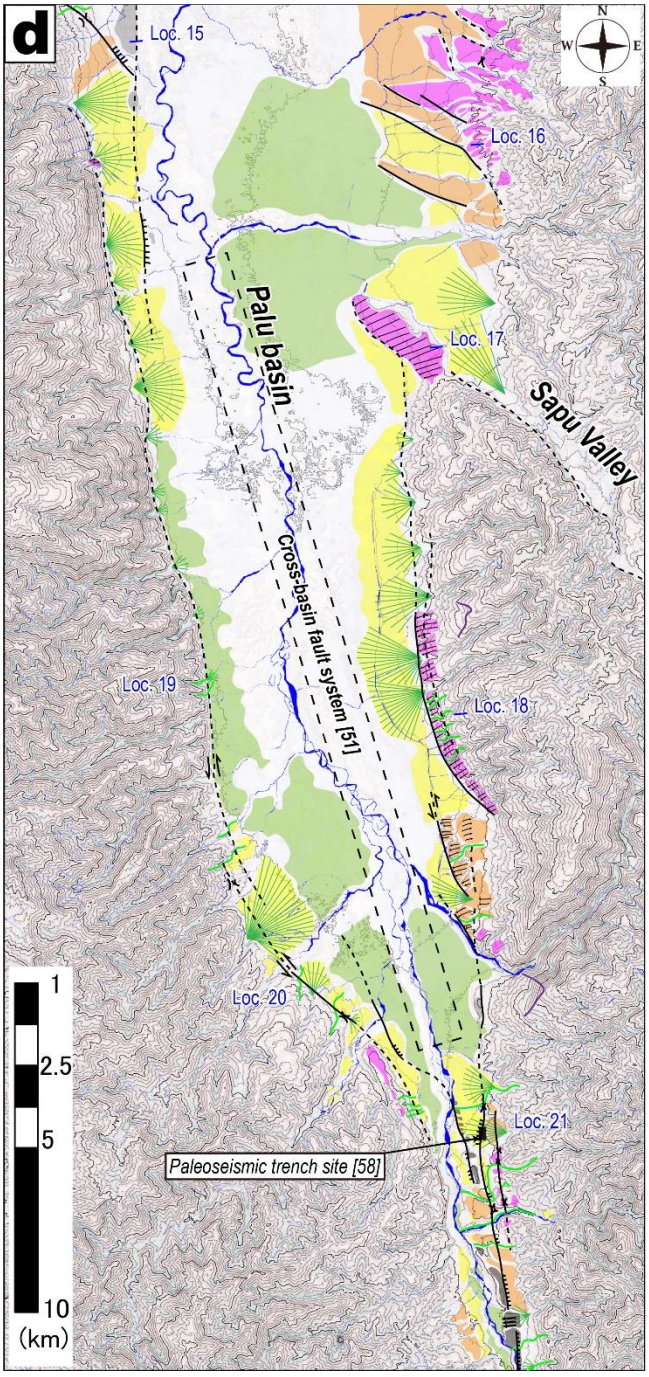

Figure 5. (continued)

Preprints (www.preprints.org) | NOT PEER-REVIEWED | Posted: 18 June 2021 doi:10.20944/preprints202106.0484.v1

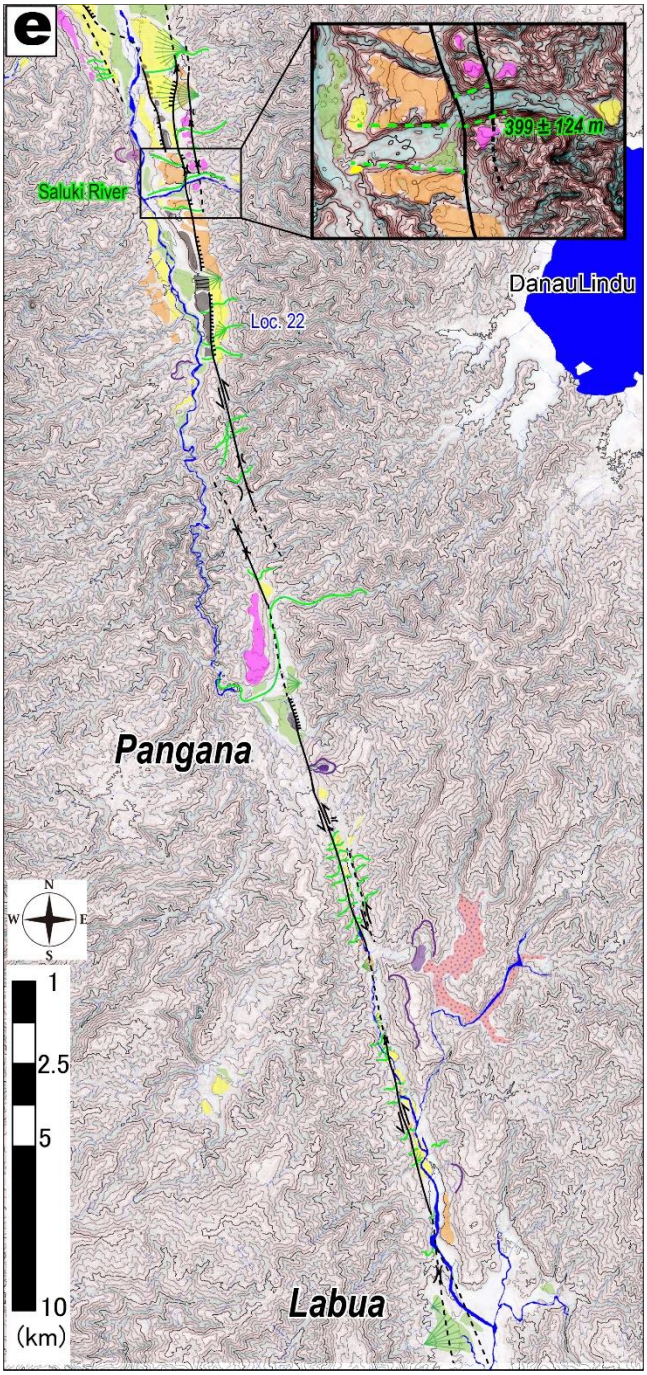

Figure 5. (continued)

The M2 surface is about 100–130 m above the modern riverbed and has a more fragmented distribution than the L1 and M1 surfaces. Uplift associated with faulting appears to have affected the preservation of the surface. Bellier et al. [53] reported ^{10}Be exposure ages of 40,000 ± 6800, 62,000 ± 11,000, and 80,000 ± 13,000 yr from gravels of a fan on the west flank of the Palu basin at elevations of 125–145 m, corresponding to the M2 terraces. However, they concluded that these ages reflected rejuvenation by reworking after the formation of the terrace surface and that the M2 terraces were abandoned at 125 ± 20 ka during MIS 6.

The H1 surface is about 170 m above the modern riverbed, and although it is widely distributed from the Tanimbaya Peninsula to the Palu basin (Figures 5a–d), it is highly fragmented in the southernmost part of the study area (Figure 5e). The H1 surface is

Preprints (www.preprints.org) | NOT PEER-REVIEWED | Posted: 18 June 2021 doi:10.20944/preprints202106.0484.v1

relatively well preserved along the coast in the northern part of the study area (Figures 5a–b), but poorly preserved in the inland part (Figures 5c–d) due to dissection. Bellier et al. [53] reported anomalously young ^{10}Be exposure ages (5000 ± 1200 yr BP) from gravel at 190 m elevation on the west flank of the Palu basin (Figure 5c). The H1 surface is likely a topographic surface that was abandoned during the 250–145 ka glacial period.

The H2 surface is mapped only in a small part of the hills east of the head of Palu Bay (Figure 5c). It is very high, more than 450 m above the modern riverbed, and its origin and the age of its abandonment are unclear.

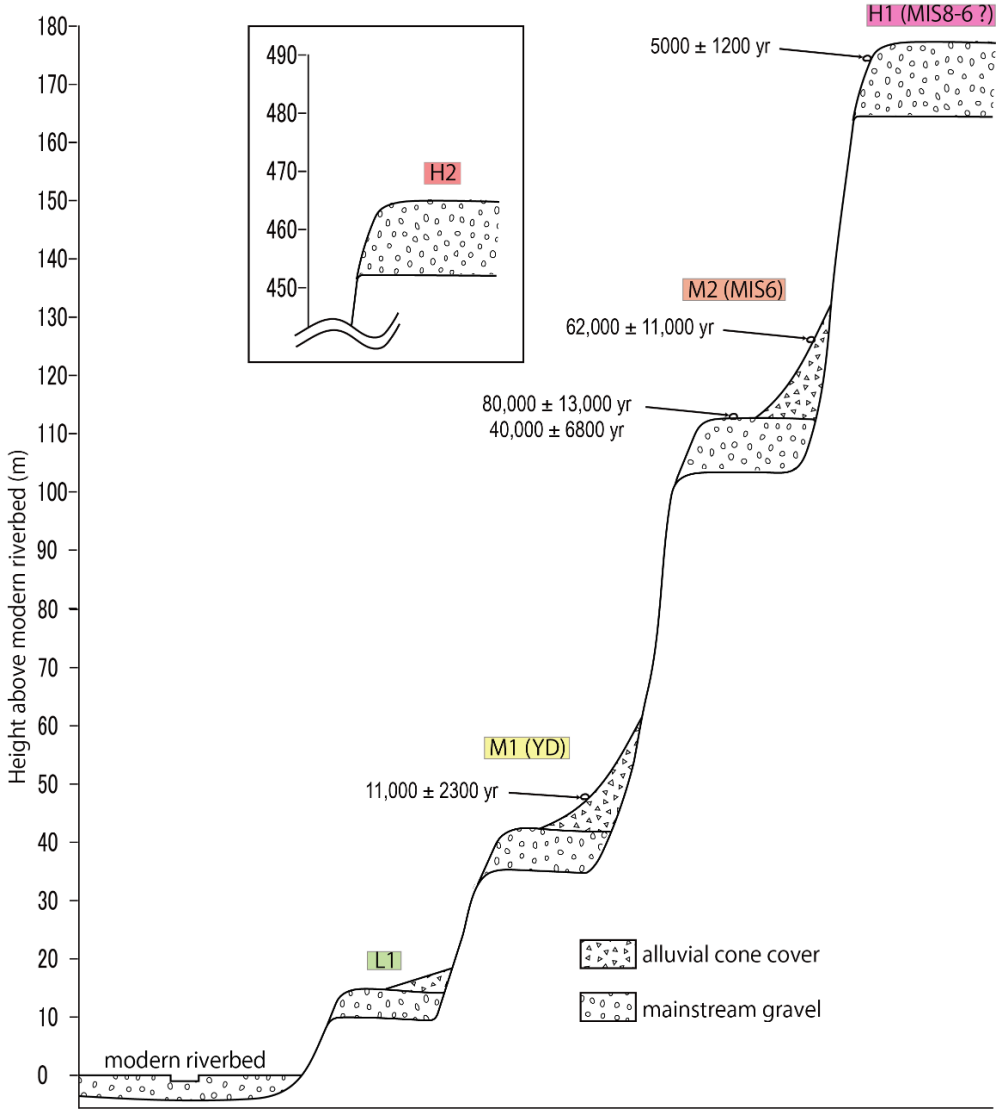

Figure 6. Schematic cross-section across fluvial terraces and alluvial fans along the Palu-Koro fault. The specific heights above the modern riverbed vary from place to place. Sediment thicknesses are not drawn to scale. Also shown are ^{10}Be exposure ages of surface gravels on the Palu basin's west flank (Figure 5c) [53]. Correlations with paleoclimatic events are also shown: MIS, marine isotopic stage; YD, Younger Dryas.

 doi:10.20944/preprints202106.0484.v1

4.2. Tectonic geomorphology

Our geomorphic mapping detected many fault scarps, flexures, tilts, systematic river offsets, wind gaps, and pressure ridges in the study area, which we used to identify geomorphically active fault traces. Here, these are described from north to south in the order of their locality (Loc.) numbers shown in Figure 5.

Near the Tanimbaya Peninsula (Figure 5a), near the epicenter of the 2018 earthquake, no distinct features of fault displacement were seen on the terrace surfaces. Nonetheless, an alignment of debris-filled valleys and multiple terrace planes (Locs. 1 and 2) and wind gaps (Loc. 3) in the inland area suggests that it was the site of faulting activity that caused relative uplift in the west, and we inferred an active fault line there. However, this presumed active fault line ends farther south near Loc. 4 (Figure 5b) as signs of activity appear on a right-offset fault segment near the coast.

Farther south, the H1 terraces form a N-S alignment near the west coast (Loc. 5, Figure 5b). Inland from these are a debris-filled valley near Loc. 6 and a wind gap near Loc. 7, defining a presumed active fault with uplift on the west side. The right-stepping arrangement of this fault segment and the segment to the north shows a sense of left-lateral displacement consistent with the Palu-Koro fault's present sense of motion, dating back as far as the time the H1 surface formed (250–145 ka).

Farther south near the head of Palu Bay, several west-facing fault scarps were identified on the terrace surface, including one on the H1 plane at Loc. 8 and another between the L1 and M2 planes at Loc. 9 (Figure 5c). The presence of these scarps implies that the fault was active after the M2 surface was abandoned (125 ± 20 ka). South of Loc. 9, distinct fault features appear on both flanks of the Palu basin (Figure 5d). On the east flank, the N-S-trending faults bend sharply just south of Loc. 10 into a set of short faults 1–6 km in length oriented northwest-southeast (Loc. 11). Left-lateral river offsets on the H1 terrace at Loc. 10 and on the M2 terrace at Loc. 11 indicate that these faults on the east flank were likely continuously active from 250 ka to 11 ka. On the west flank, several faults show strong left-lateral displacement. A river crossing an alluvial fan correlated with the M1 terrace at Loc. 13 is laterally displaced more than 300 m, from which an average slip rate of 35 ± 8 mm/yr has been estimated [54]. On the mountainside near Loc. 14, a fault displaces a river that dissects the H1 terrace, and two other faults that border the H1 and M1 terraces have east-facing scarps. To the south, the faults bend to southeast and display a stairstep series of east-facing scarps near the sampling point of Bellier et al. [53]. Also, Patria and Putra [31] pointed out that several pressure ridges in the interior of the basin from Palu Bay to Loc. 15 (Figure 5c), but we could not determine whether they are pressure ridges with certainty, except for the clear one in Loc. 15.

Toward the south, tectonic features continue on both flanks of the Palu basin (Figure 5d). On the east side, several short, parallel faults about 1.5 to 5 km long and trending NW-SE are present at Loc. 16 with downdropped western sides. These faults displace the H1, M2, and M1 planes, suggesting that they were active between 250 and 11 ka. At Loc. 17, the relatively well-preserved surface of the H1 plane dips about 8% (4.5°) toward the southwest. Although we cannot rule out the possibility that this tilt is an original feature, it may result from repeated faulting. South of Loc. 17, the basin-bounding fault divides into a southward-continuing fault and an eastward splay mapped as the Sapu Valley fault system [51]. From Loc. 17 to Loc. 18, a series of fresh alluvial fans are classified as M1 terraces, but they display no clear fault scarps. However, the well-developed H1 terraces around Loc. 18 display westward flexural deformation, and the rivers that dissect the H1 terraces show consistent left-lateral displacement, suggesting that there are two parallel faults in this section. On the west flank, some fresh pressure ridges and east-facing fault scarps appear on the M1 terraces south of Loc. 15, and the presumed active fault is mapped on the M1 terrace. Around Loc. 19, the mountain-basin boundary is well defined but alluvial fans are poorly developed, implying that subsidence to the west exceeded the

 doi:10.20944/preprints202106.0484.v1

sediment supply. Watkinson and Hall [51] pointed out that the flow paths of meandering rivers are regulated in a straight line and that a cross-basin fault system is hidden inside the basin (Figure 5d). However, decisive features such as fault scarps and lateral offset of tributaries could not be extracted from the basin interior by our topographic interpretation. The presumed active fault continues south and curves eastward around Loc. 20. In the vicinity of Loc. 20, the rivers on the alluvial fan that constitutes the M1 terraces show left-lateral displacement, suggesting that the fault has been active repeatedly since at least the abandonment of the M1 terrace (11,000 ± 2300 yr). The faults on the east and west flanks converge at the south end of the basin near Loc. 21, where the presence of several systematic lateral river offsets and pressure ridges upon terraces suggests a very high average displacement rate. Here the sides of the M2 terraces, where they are dissected by Saluki River, preserve evidence of 399 ± 124 m of lateral displacement (Figure 5e inset). Based on this displacement, the average slip rate is 3.44 ± 1.54 mm/yr when determined from the age of the higher M2 terrace and 40.40 ± 17.72 mm/yr when determined from the age of the lower M1 terrace. The true mean slip rate at this site must lie between these two values [73], but given the heavy rainfall and vigorous erosion in this tropical region, the higher value in the range is more likely. This value is in good agreement with slip rates estimated in previous studies, such as 35 ± 8 mm/yr on the west side of the Palu basin [54] and ~40 mm/yr revealed by GPS observations [44, 55–57]. Furthermore, of the three parallel faults in the vicinity of Loc. 21, a trench survey conducted on the middle fault identified a total of five paleoseismic events in the past 700 years, including the 2018 earthquake [58]. Therefore, of the three parallel faults near Loc. 21, it is likely that the middle fault was used to release strain in relatively recent times.

From the south end of the Palu basin to its end at Labua, the Palu-Koro fault strikes N15°W and is relatively linear (Figure 5e). A well-formed, continuous pressure ridge on the M1 terrace near Loc. 22 indicates that this part of the fault has experienced repeated displacement at least since the abandonment of the M1 terrace (11,000 ± 2300 yr). The active trace steps to the right south of Loc. 22, and in the vicinity of Pangana, a pressure ridge and a west-facing fault scarp are present in a debris-filled valley. Between Pangana and Labua, alluvial fans equivalent to M1 or M2 terraces are present along the valleys, and the tributary rivers that dissect them display systematic left-lateral displacement.

4.3. Optical correlation and vector field results

Our optical correlation analysis revealed a linear discontinuity of N-S displacement extending about 150 km from the epicentral area of the 2018 earthquake to the south of Labua. The absolute value of the displacement shows positive (northward) in the whole area (Figure 7a), which is unnatural and may be due to the ortho-correlation of Sentinel-2 at Level-1C. The relative displacements show that the east side moves to the north, and the west side moves to the south across the optical discontinuity. Indications of surface ruptures appeared in a segment 65 km long between the north end of Palu Bay and the area south of Pangana. The largest N-S displacement was 5.0–5.5 m (see profiles B-B′ and C-C′ in Figure 8), which is likely an underestimate compared to the largest lateral displacement of about 6 m measured in the field [30, 32, 33] and is probably due to the strikes slightly west of north. Areas to the north and south of this section, however, display fragmentary color contrasts but no clear discontinuities. Profiles A–A′ and E–E′ in these respective areas (Figure 8) show broadly distributed N-S displacements of about 2 m and suggest that coseismic slip did not reach the surface.

Preprints (www.preprints.org) | NOT PEER-REVIEWED | Posted: 18 June 2021 doi:10.20944/preprints202106.0484.v1

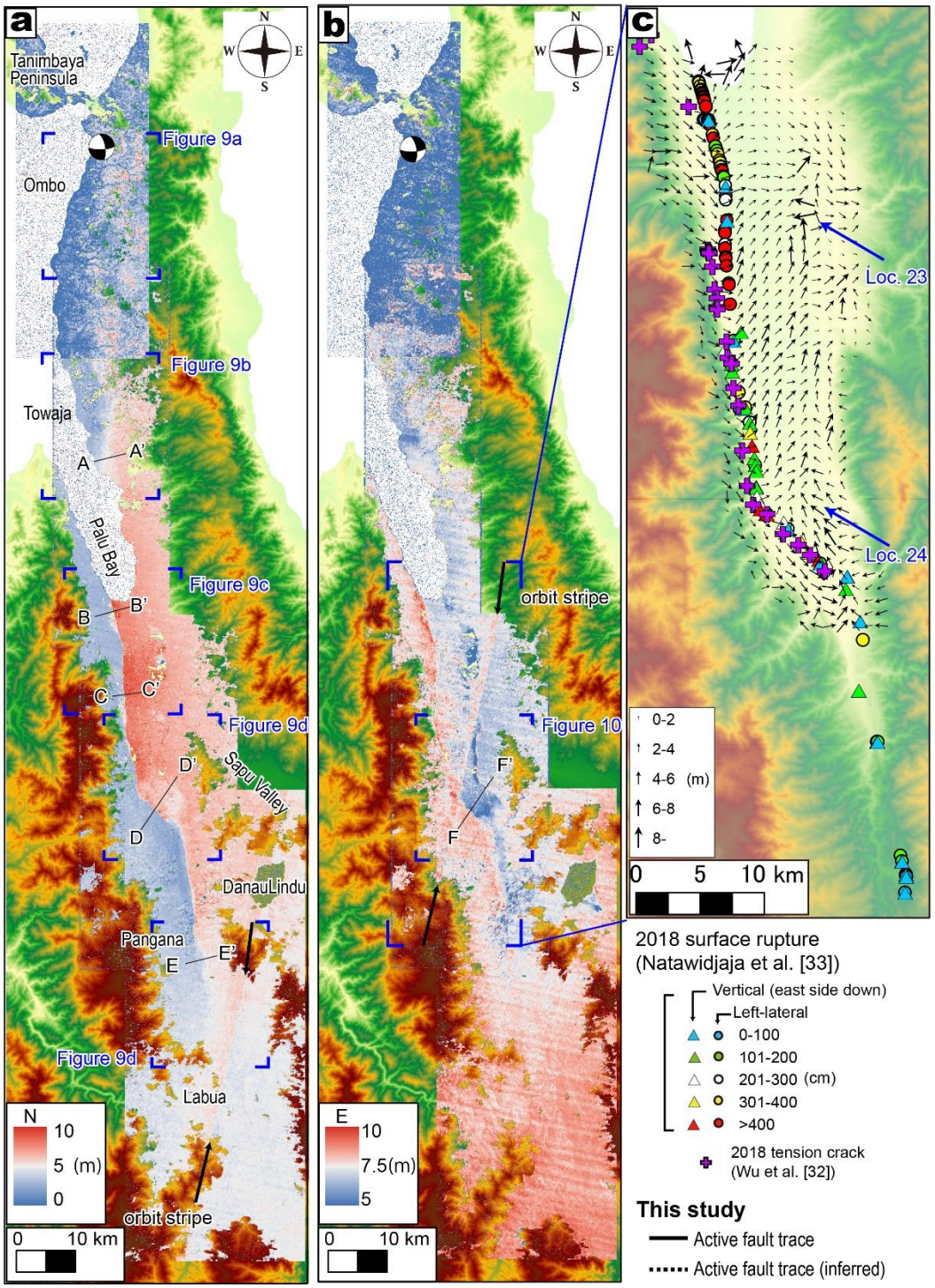

Figure 7. (a) Distribution of horizontal displacement in the N-S direction by optical correlation of Sentinel-2 images (Table 1). The area is the same as in Figure 3. (b) Horizontal displacement distribution in the E-W direction. Profiles A–A′ to F–F′ are shown in Figure 8. (c) Vector field based on the optical correlation result of SPOT-6 images (Table 2). The grid size of the vectors is 1 km. The original optical correlation results used in the field are shown in Data S2 in the Supplementary Materials. The 2018 surface ruptures and tension cracks based on the field surveys [32, 33] are also shown.

Preprints (www.preprints.org) | NOT PEER-REVIEWED | Posted: 18 June 2021 doi:10.20944/preprints202106.0484.v1

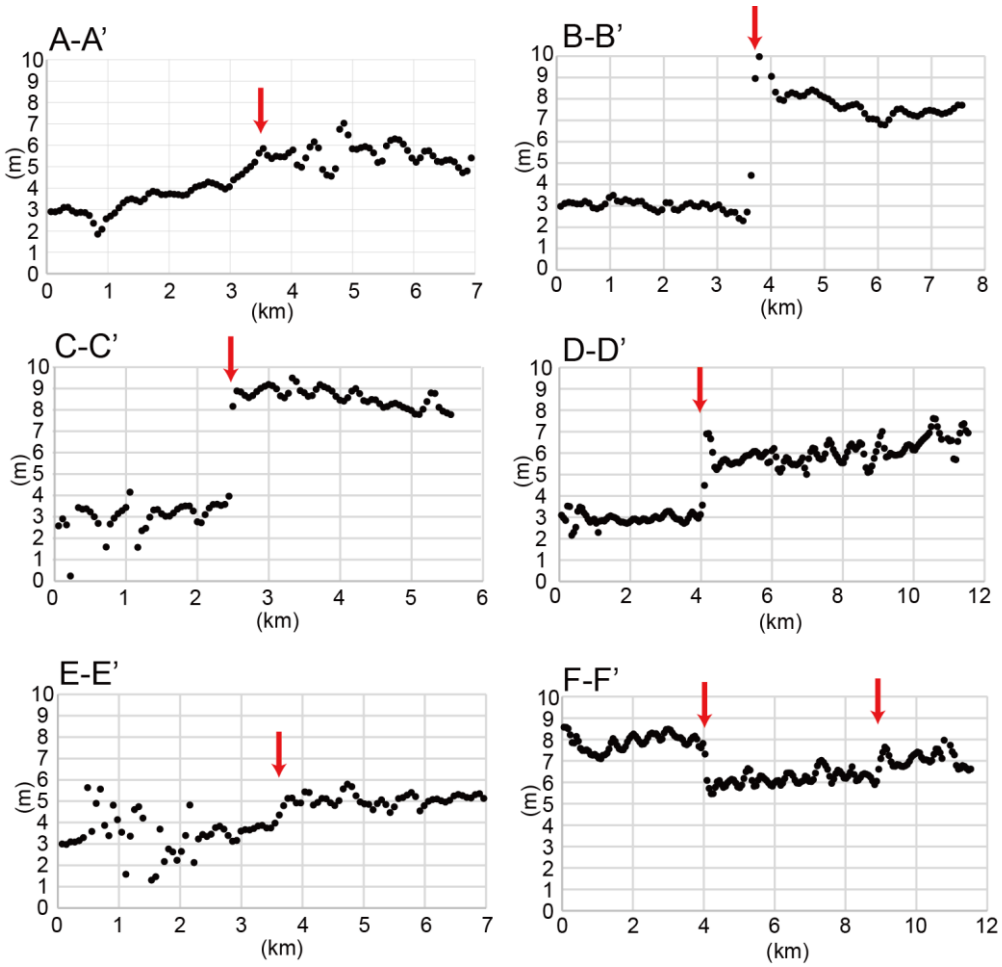

Figure 8. Profiles of horizontal displacement in the N-S direction (A–A′ to E–E′) and the E-W direction (F–F′). Profile lines are shown in Figures 7a and 7b. Red arrows denote identified surface ruptures.

The distribution of E-W displacement (Figure 7b) also features a linear discontinuity extending from Palu Bay to Pangana, although it is weak and fragmented compared to the N-S displacement distribution. All absolute values show eastward displacement, which is also considered to be an unnatural value due to orthorectification errors in Sentinel-2. The relative displacements show that the east side across the optical discontinuity shows a more significant east displacement than the west side.

In the vector field (Figure 7c) within the Palu Basin generated from SPOT-6 optical correlation, the eastern basin shows a sense of relatively northeastward movement, and the western basin shows a sense of southeastward movement after the appearance of the surface ruptures. The vectors within the basin do not uniformly show the northeast direction; for example, near Loc. 23 on the northeast side of the basin, the vectors show random disturbance. An area around Loc. 24 in the deep (southern) part of the basin shows a similar disturbance zone. They are possible that non-tectonic phenomena, different from elastic deformation associated with fault movement.

5. Discussion

5.1. Comparison of optical correlation results and tectonic geomorphology

With our geomorphic observations and optical correlation results, we can compare our geomorphically active fault traces with the surface ruptures from the 2018 earthquake.

 doi:10.20944/preprints202106.0484.v1

Comparisons with the surface ruptures mapped by field surveys [30–33] may also shed light on the development of the Palu basin in the Palu-Koro fault system.

Optical correlation documented slight left-lateral displacement around Ombo, near the epicenter (Figures 7a and 9a). Because the linear discontinuity of this displacement is indistinct, it is unlikely that a surface rupture occurred there. Furthermore, this discontinuity does not coincide with any of the geomorphically active fault lines in this study, indicating that these faults were not activated during the 2018 earthquake. The presence of the 2018 rupture on the floor of Palu Bay suggests that current activity on the Palu-Koro fault has shifted to the west [33]. We interpret the geomorphically active faults near Ombo as inactive en-echelon basin sidewall faults (Figure 1a) [8]. Fragmentary surface ruptures associated with the 2018 earthquake described near Ombo [30] do not correspond to the lineaments identified by optical correlation; they are more likely to be passive and gravitational ruptures associated with seismic shaking and static crustal strain.

Farther south, around Towaja, optical correlation shows a relatively clear linear discontinuity indicating left-lateral displacement broadly consistent with the seismic mechanism of the 2018 earthquake (Figures 7a and 9b). Field surveys around Towaja also reported 2018 surface ruptures with left-lateral displacement [30, 32]. However, these ruptures lie west of the optical discontinuity (Figure 9b) and may be nontectonic displacements. The linear discontinuity is oblique to the geomorphically inferred active fault. This may be due to the possibilities that (1) a new fault is growing that connects the seafloor fault in Palu Bay [32] with the presumed active fault to the east, and/or (2) fault-related features are obscured by sediment supplied from highlands to the east.

The largest displacements of the 2018 ruptures were recorded 20 km south of Palu Bay on the west flank of the Palu basin [30, 32, 33] at a location that almost perfectly coincides with the optical discontinuity (Figures 7a and 9c). The geomorphically active faults are located farther west in the highlands and appear to be right-stepping en-echelon faults and tension cracks on these active faults have been recognixed by field survey [32]. However, both N-S and E-W results failed to detect discontinuities corresponding to these tension cracks (Figures 7a, 7c, and 9c). Therefore, the tension cracks detected by the field survey [32] are of a scale that cannot be detected by optical correlation, and we interpret these faults as having been abandoned, and current activity appears to have shifted to basin-shortcut faults (Figure 1b) and relay ramps (Figure 1c) in the interior of the Palu basin (Figures 5c and 9c). The presence of several pressure ridges between Palu Bay and Loc. 15 [31] suggests that this basin-shortcut fault has been active at least several times since the abandonment of the L1 terrace (7–5 ka). Yet the mountainside fault has a very high average slip rate of 35 ± 8 mm/yr since the M1 abandonment (11,000 ± 2300 yr) (Figure 5c), and paleoseismic trenching indicates that the most recent previous surface rupture event on it occurred at 900–800 yr BP [52, 54]. In other words, the 2018 event may be the first major earthquake that fault activity had moved from the mountains to the interior of the basin.

Similarly, there is an area farther south in the Palu basin (Figure 9d) where the geomorphically active faults and the 2018 ruptures are far apart. The faults on the basin's flanks converge here (Figure 5d), but optical correlation and the field survey [32, 33] both indicate that the mountainside faults have been abandoned and the 2018 earthquake activated new shortcut faults in the basin. Although the 2018 surface ruptures in the basin appear on the L1 terraces, no fault-related geomorphic features are discernible on the L1 terrace (Figure 5d), which implies that these surface ruptures are the first to appear here since abandonment of the L1 terrace (7–5 ka).

Preprints (www.preprints.org) | NOT PEER-REVIEWED | Posted: 18 June 2021 doi:10.20944/preprints202106.0484.v1

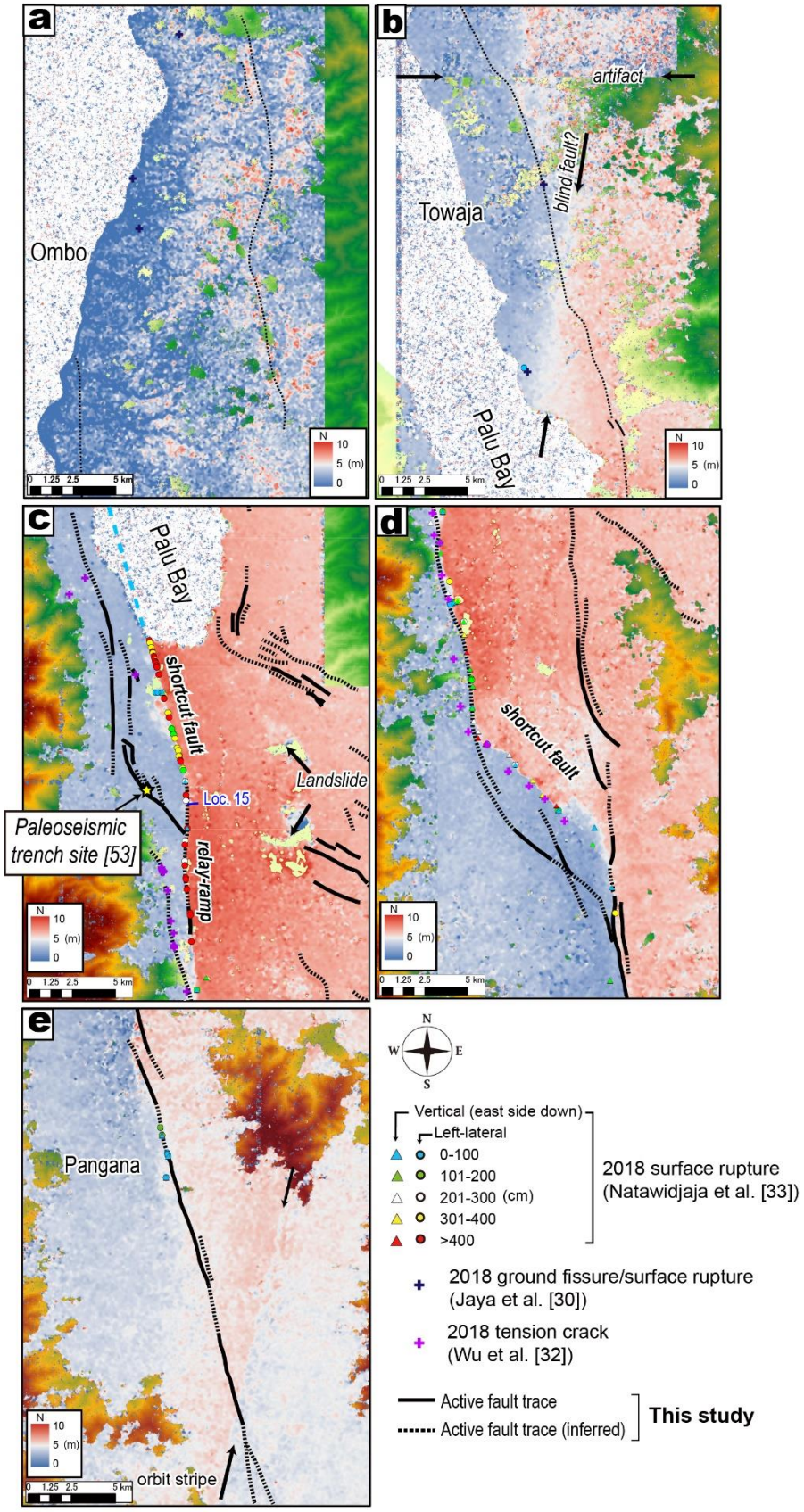

Figure 9. Horizontal displacement in the N-S direction (colors); also shown are active fault traces identified by geomorphic observation (black lines) and the location of 2018 surface ruptures or tension cracks confirmed in field surveys [30, 32, 33] (symbols). Panel locations are shown in Figure 7a.

 doi:10.20944/preprints202106.0484.v1

The southern end of the 2018 surface ruptures mapped by field surveys is located around Pangana [30, 32, 33], consistent with our optical correlation results (Figure 9e). The locations of the geomorphically active faults and the 2018 surface ruptures are generally consistent with each other, suggesting that the same fault plane is repeatedly active in the inland mountains. The displacements measured in the field near Pangana are about 30–60 cm [33], which suggests that, where the fault strikes as close to N-S as possible, the optical correlation technique using Sentinel-2 imagery may be able to extract surface displacements with 30–60 cm accuracy.

We can compare the above results with the pull-apart basin model [8] shown in Figure 1. For example, the abandonment of mountainside faults and the activity of basin-shortcut faults (Figure 9d) inferred on the west flank of the Palu basin are consistent with the stages shown in Figures 1b and 1c. The abandonment of the en-echelon basin sidewall faults and the appearance of basin-shortcut faults and relay ramps in the northern part of the basin near Palu Bay (Figure 9c) is consistent with the stage shown in Figure 1c. Thus, the Palu basin is in a relatively mature stage of the pull-apart basin. If the Palu-Koro fault continues to develop in accordance with this model, the abandoned mountainside faults are unlikely to be reactived in future earthquakes, and only basin-shortcut faults will be activated to release lateral displacement.

5.2. Lateral spreading phenomena occurring at the pull-apart basin

In the N-S displacement map of the Palu basin (Figure 9c), left-lateral basin-shortcut faults appear on the west flank, but there is no evidence of activity along the east flank. According to the optical correlation result, some blank areas on the northeast side of the basin show no correlation (Figure 9c). The vector field also shows that the random ground moves (around Loc. 23 in Figure 7c), indicating that this area was subject to liquefaction landslides that caused extensive damage. Bradley et al. [27] and Watkinson and Hall [28] pointed out that the rise in groundwater level due to irrigation caused landslides on gentle slopes of only about 1°. Masson et al. [29] mentioned that these landslides coincided with the alluvial fans' terminal part.

In the N-S displacement map of the southern Palu basin (Figure 9d), left-lateral basin-shortcut faults appear on the west flank, but there is activity along the east flank. On the other hand, the E-W displacement map shows a linear discontinuity in the basin about 1.0–1.5 km west of the geomorphically active fault trace on the east flank, from which it appears that an area of about 79,000 m^2 moved westward relatively as a block by about 1–2 m (Figure 10a). The detailed vector field shows disturbance in the basin although the overall trend towards the north (Figure 10b). This movement cannot be explained by crustal deformation caused by the 2018 surface rupture and may indicate lateral flow phenomenon similar to those on the basin's northwest (around Loc. 23 in Figures 7c and 9c). Nevertheless, this phenomenon is called “lateral spreading” in this study to distinguish it from the northwest part of the basin because of its more extensive scale. The linear discontinuity in E-W displacement on the east flank corresponds well with the alluvial fan’s terminal part on the east flank (Figure 11). This is consistent with the characteristics of liquefaction landslides as pointed out by Masson et al. [29]. Although shaking-related landslides have not been reported in the southern Palu basin, lateral spreading may have occurred there by similar mechanisms. Similar lateral spreading on flat or gently sloping surfaces during earthquakes has also been reported in Aso caldera, Japan, during the 2016 Kumamoto earthquake [74, 75]. Some have argued on the basis of cumulative activity that the lateral spreading of the Aso caldera is a tectonic active fault [76]. It can be difficult to distinguish among tectonic and nontectonic linear discontinuities and lateral flow phenomena, but it should be noted that similar phenomena occur around the margins of pull-apart basins.

Preprints (www.preprints.org) | NOT PEER-REVIEWED | Posted: 18 June 2021 doi:10.20944/preprints202106.0484.v1

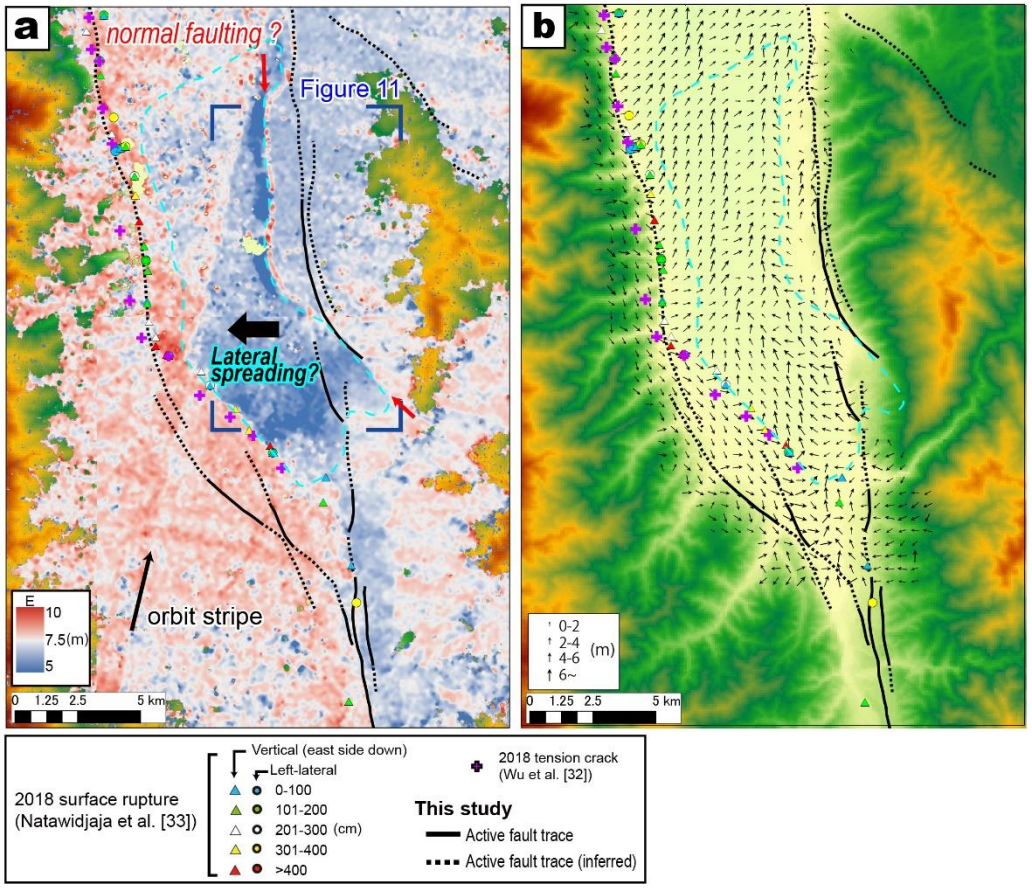

Figure 10. Horizontal displacement in the E-W direction around the southern Palu basin (location in Figure 7b). Geomorphically active fault traces and 2018 surface ruptures and tension cracks [30, 32, 33] are also shown. (b) Vector field of the same area. The grid size of the vectors is 500 m. Base results of the optical correlation of SPOT-6 images are shown in Data S2 in Supplementary Materials.

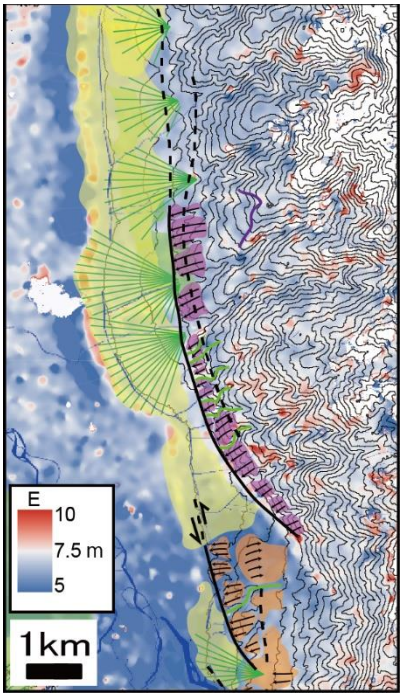

Figure 11. Superimposes geomorphic information and topographic contours (from Figure 5d) on an enlarged portion of the Figure 10a.

 doi:10.20944/preprints202106.0484.v1

5.2. Lessons from the 2018 Palu earthquake

The 2018 Palu earthquake produced surface ruptures in several locations inside the basin that did not correspond to geomorphically active faults; however, these do correspond to elements of the pull-apart basin model shown in Figure 1 [8]. Similar instances have been reported elsewhere in the world. For example, basin-shortcut faults were identified in the Haiyuan fault system, China, where they were interpreted as part of the pull-apart basin's terminal stage [6]. The left-lateral Dead Sea fault system has two distinct pull-apart basins, the Dead Sea Basin and Elat Bay, where en-echelon basin-margin faults and short fault clusters have been identified [77–80]. The 2018 Palu earthquake is the first time to our knowledge that a fault field has been observed transitioning into a pull-apart basin, and the characteristics of the surface ruptures from the Palu earthquake may be useful in anticipating surface ruptures in other pull-apart basins. For example, the Lake Suwa basin along the Itoigawa-Shizuoka Tectonic Line in Japan (Figure 12) is a distinct pull-apart basin and is one area where the estimated risk of near-future earthquakes is increasing. According to the Headquarters for Earthquake Research Promotion [81], the probability of a major earthquake occurring in the central section of the tectonic line within the next 30 years is 0.9–8.0% based on trenching studies documenting the paleoearthquake history. In the Lake Suwa area, two groups of active dip-slip faults have been identified, the Suwako Nangan faults to the southwest and the Suwako Hokugan faults to the northeast [82–84]. Both fault groups converge southeastward into the co-linear left-lateral Chino and Aoyagi faults [85]. Further to the southeast, the Oosawa and Wakamiya faults exhibit Riedel-shear pop-up structures on their southwest slopes [86]. The characteristics of these active faults are similar to those of the Palu-Koro fault system, and it should be noted that coseismic offsets on basin-shortcut faults and lateral spreading of alluvial fans (Figure 13) may occur in the Lake Suwa area during the next major earthquake there. Borehole investigations [83] and seismic reflection survey [87] in the Lake Suwa basin have suggested the presence of blind and flower-structural faults within the basin, which may represent basin-shortcut faults that have been active recently. Many rivers pour into Lake Suwa from the surrounding area, and the basin is in wet condition. Therefore, there is a high risk of coseismic lateral spreading as in the 2018 Palu earthquake.

In the Palu basin, Watkinson and Hall [51] predicted the existence of hidden faults in the basin from the width of the meandering rivers is regulated in a straight line (Figure 5d). Some basin-shortcut faults that are accompanied by weak fault scarps or pressure ridges (e.g., Loc. 15 in Figure 5c) could have been mapped as if they had used high-precision DEM data, they might have been able to predict the detailed location of the basin shortcut fault before the 2018 earthquake. The tectonic geomorphology of pull-apart basins should be evaluated on the basis of high-precision topographic data with a developmental model (Figures 1 and 13) in mind.

Preprints (www.preprints.org) | NOT PEER-REVIEWED | Posted: 18 June 2021 doi:10.20944/preprints202106.0484.v1

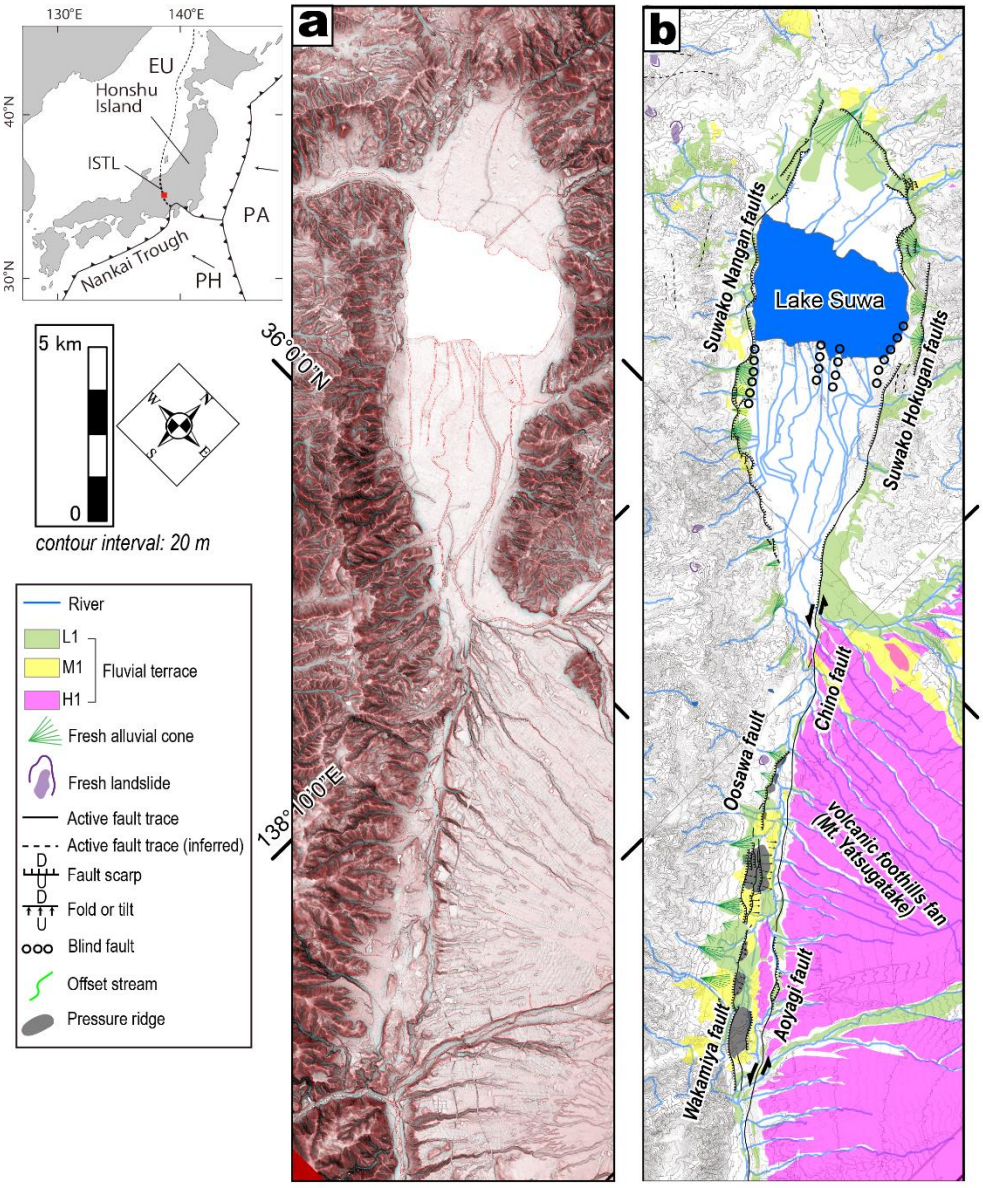

Figure 12. (a) MPI-RRIM of the area around Lake Suwa along the Itoigawa-Shizuoka Tectonic Line, central Japan, based on the 5-m-grid DEM of the Geospatial Information Authority of Japan. (b) Geomorphic map and distribution of active faults [82–86] in the same area.

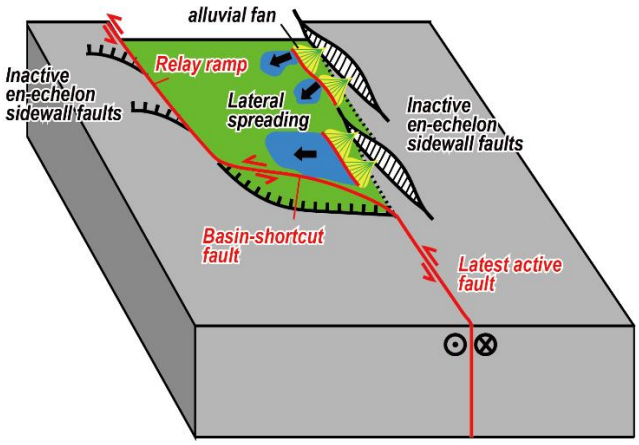

Figure 13. Schematic illustration of a pull-apart basin showing active features including basin-shortcut faults, relay ramps, and lateral spreading.

6. Conclusions

The 26 September 2018 Palu earthquake (Mw 7.5) produced 180 km of surface ruptures along the Palu-Koro fault system on land and on the seafloor. This study used stereopairs of MPI-RRIMs to visualize the topography and map the geomorphically active faults in the Palu-Koro fault system. We also used optical correlation of Sentinel-2 and SPOT-6 satellite imagery to map the surface ruptures and surface deformation caused by the 2018 earthquake.

Our geomorphic analysis revealed multiple terrace surfaces and overlying alluvial fans. By correlation with terraces dated by ^{10}Be age classification in previous studies, we were able to interpret these terraces as features of climate-related origin corresponding to specific marine isotope stages. Deformational geomorphic features of these terraces, such as fault scarps, flexures, pressure ridges, systematic river offsets, and wind gaps, enabled us to map detailed traces of the Palu-Koro fault. By comparing these fault traces with the locations of the 2018 ruptures and our optical correlation results, we showed that some surface ruptures on the west flank of the Palu basin do not match the geomorphic fault trace. In terms of the analog model of pull-apart basin development, the Palu basin is mature, such that the en-echelon basin sidewall faults at the mountain-basin boundary were inactive in the 2018 earthquake while the basin-shortcut faults and relay ramps in the basin displayed the greatest coseismic activity. Previous field surveys reported a damaging landslide in the northern part of the Palu basin, and our optical correlation and its vector field also suggest that large-scale lateral spreading in a direction unrelated to the fault displacement occurred in the southern Palu basin.

Although pull-apart basins exist throughout the world and their development typically occurs on the scale of tens of thousands of years or more, the 2018 Palu earthquake revealed a snapshot of a transitional stage in which en-echelon basin sidewall faults that were active during the previous large earthquake were abandoned and an incipient area of fault activity existed in the basin interior that was not yet evident in the topography. Our findings may be of importance in reducing hazards associated with surface ruptures; for example, at Lake Suwa, Japan, in a tectonic setting similar to that of the Palu-Koro fault system, it may be possible to anticipate the locations of surface ruptures that may appear in the near future. Future studies of pull-apart basins based on the developmental model of the pull-apart basin and informed by this case study of the 2018 Palu earthquake may yield new and significant results wherever high-precision topographic data are available.

Supplementary Materials: The following are available online at www.mdpi.com/xxx/s1:

Data S1 (zip files). Stereopaired MPI-RRIMs corresponding to Figure 5 in the text. To perform stereoscopic observations using MPI-RRIMs, the free software StereoPhoto Maker (http://stereo.jpn.org/eng/stphmkr/index.html, last accessed March 2021) and the Pocket 3Dvu stereoscope (http://www.berezin.com/3d/pocket_3dvu.htm, last accessed March 2021) are required. For more details on stereopaired MPI-RRIMs and their use, see ref. [59].

Data S2 (pdf). (a) ArcGIS model builder flow for creating vector fields. The ellipse represents the input data, the blue ellipse represents the input parameter ("P" means parameter), and the rectangle represents the tool to be executed, respectively. (b) N-S displacement and (c) E-W displacement maps from SPOT-6 images used to create the vector field.

Data S3 (kmz file). Active fault traces identified in this study.

Author Contributions: Conceptualization, K.K.; Methodology, K.K. and J.S.; Visualization, K.K.; Writing - original draft, K.K.; Writing - review & editing, K.K. and J.S.; All authors have read and agreed to the published version of the manuscript.

Funding: This work was financially supported in part by the Central Research Institute of Electric Power Industry (CRIEPI) under its "Fault survey for recent earthquakes" program.

Data Availability Statement: Not applicable.

Acknowledgments: We thank Keiichi Ueta and Yasuhira Aoyagi (CRIEPI) for useful discussions about the analog model of the pull-apart basin and vector field. The DEM data used in this study were provided by the Geospatial Information Agency (BIG) of Indonesia (http://tides.big.go.id/DEMNAS/index.html) and the Geospatial Information Authority of Japan. The MPI-RRIM image was produced by the DEM visualization method of Asia Air Survey Co., Ltd. (protected by Japanese Patents No. 3670274 and 4272146 but open to academic use).

Conflicts of Interest: The authors declare no conflict of interest.

References

1. Burchfiel, B.C., Stewart, J.H., 1966. "pull-apart" origin of the central segment of Death Valley, California. Bull. Geol. Soc. Am. 77, 439–442. https://doi.org/10.1130/0016-7606(1966)77[439:POOTCS]2.0.CO;2
2. Crowell, J.C., 1974. Sedimentation Along the San Andreas Fault, California, in: Modern and Ancient Geosynclinal Sedimentation. pp. 292–303. https://doi.org/10.2110/pec.74.19.0292
3. Garfunkel, Z., 1981. Internal structure of the Dead Sea leaky transform (rift) in relation to plate kinematics. Tectonophysics 80, 81–108. https://doi.org/10.1016/0040-1951(81)90143-8
4. Aydin, A., Nur, A., 1982. Evolution of pull-apart basins and their scale independence. Tectonics 1, 91–105. https://doi.org/10.1029/TC001i001p00091
5. Mann, P., Hempton, M.R., Bradley, D.C., Burke, K., 1983. Development of pull-apart basins. J. Geol. 91, 529–554. https://doi.org/10.1086/628803
6. Peizhen Zhang; Burchfiel, B.C.; Shefa Chen; Qidong Deng Extinction of pull-apart basins. Geology 1989, 17, 814–817, doi:10.1130/0091-7613(1989)017<0814:EOPAB>2.3.CO;2. 1.
7. McClay, K., Dooley, T., 1995. Analogue models of pull-apart basins. Geology 23, 711–714. https://doi.org/10.1130/0091-7613(1995)023<0711:AMOPAB>2.3.CO;2
8. Wu, J.E., McClay, K., Whitehouse, P., Dooley, T., 2009. 4D analogue modelling of transtensional pull-apart basins. Mar. Pet. Geol. 26, 1608–1623. https://doi.org/10.1016/j.marpetgeo.2008.06.007
9. Dooley, T., McClay, K., 1997. Analog modeling of pull-apart Basins. Am. Assoc. Pet. Geol. Bull. 81, 1804–1826. https://doi.org/10.1306/3b05c636-172a-11d7-8645000102c1865d
10. Rahe, B., Ferrill, D.A., Morris, A.P., 1998. Physical analog modeling of pull-apart basin evolution. Tectonophysics 285, 21–40. https://doi.org/10.1016/S0040-1951(97)00193-5
11. Sims, D., Ferrill, D.A., Stamatakos, J.A., 1999. Role of a ductile decollement in the development of pull-apart basins: Experimental results and natural examples. J. Struct. Geol. 21, 533–554. https://doi.org/10.1016/S0191-8141(99)00010-3
12. Dooley, T.P., Schreurs, G., 2012. Analogue modelling of intraplate strike-slip tectonics: A review and new experimental results. Tectonophysics. https://doi.org/10.1016/j.tecto.2012.05.030
13. Sugan, M., Wu, J.E.L., McClay, K., 2014. 3D analogue modelling of transtensional pull-apart basins: Comparison with the Cinarcik basin, Sea of Marmara, Turkey. Boll. di Geofis. Teor. ed Appl. 55, 699–716. https://doi.org/10.4430/bgta0129
14. Corti, G., Nencini, R., Skyttä, P., 2020. Modelling the influence of pre-existing brittle fabrics on the development and architecture pull-apart basins. J. Struct. Geol. 131. https://doi.org/10.1016/j.jsg.2019.103937
15. Rodgers, D.A., 1980. Analysis of Pull-Apart Basin Development Produced by En Echelon Strike-Slip Faults, in: Sedimentation in Oblique-Slip Mobile Zones. Wiley, pp. 27–41. https://doi.org/10.1002/9781444303735.ch3
16. Katzman, R., Ten Brink, U.S., Jian Lin, 1995. Three-dimensional modeling of pull-apart basins: implications for the tectonics of the Dead Sea Basin. J. Geophys. Res. 100, 6295–6312. https://doi.org/10.1029/94JB03101
17. Kusumoto, S., Fukuda, Y., Takemura, K., Takemoto, S., 2001. Forming Mechanism of the Sedimentary Basin at the Termination of the Right-lateral Left-stepping Faults and Tectonics around Osaka Bay. J. Geogr. (Chigaku Zasshi) 110, 32–43. https://doi.org/10.5026/jgeography.110.32 (in Japanese with English abstract)
18. van Wijk, J., Axen, G., Abera, R., 2017. Initiation, evolution and extinction of pull-apart basins: Implications for opening of the Gulf of California. Tectonophysics 719–720, 37–50. https://doi.org/10.1016/j.tecto.2017.04.019
19. Liu, Y., Konietzky, H., 2018. Particle-Based Modeling of Pull-Apart Basin Development. Tectonics 37, 343–358. https://doi.org/10.1002/2017TC004685
20. Schattner, U., Weinberger, R., 2008. A mid-Pleistocene deformation transition in the Hula basin, northern Israel: Implications for the tectonic evolution of the Dead Sea Fault. Geochemistry, Geophys. Geosystems 9. https://doi.org/10.1029/2007GC001937
21. Quennell, A.M., 1958. The structural and geomorphic evolution of the dead sea rift. Q. J. Geol. Soc. London 114, 1–24. https://doi.org/10.1144/gsjgs.114.1.0001

22. Freund, R., Garfunkel, Z., Zak, I., Goldberg, M., Weissbrod, T., Derin, B., Bender, F., Wellings, F.E., Girdler, R.W., 1970. The Shear along the Dead Sea Rift [and Discussion]. Philos. Trans. R. Soc. London A Math. Phys. Eng. Sci. 267, 107–130.
23. Aragón-Arreola, M., Morandi, M., Martín-Barajas, A., Delgado-Argote, L., González-Fernández, A., 2005. Structure of the rift basins in the central Gulf of California: Kinematic implications for oblique rifting. Tectonophysics 409, 19–38. https://doi.org/10.1016/j.tecto.2005.08.002
24. Aragón-Arreola, M., Martin-Barajas, A., 2007. Westward migration of extension in the northern Gulf of California, Mexico. Geology 35, 571–574. https://doi.org/10.1130/G23360A.1
25. Seiler, C., Fletcher, J.M., Quigley, M.C., Gleadow, A.J.W., Kohn, B.P., 2010. Neogene structural evolution of the Sierra San Felipe, Baja California: Evidence for proto-gulf transtension in the Gulf Extensional Province? Tectonophysics 488, 87–109. https://doi.org/10.1016/j.tecto.2009.09.026
26. Dorsey, R.J., Umhoefer, P.J., 2012. Influence of Sediment Input and Plate-Motion Obliquity on Basin Development Along an Active Oblique-Divergent Plate Boundary: Gulf of California and Salton Trough, in: Tectonics of Sedimentary Basins: Recent Advances. pp. 209–225. https://doi.org/10.1002/9781444347166.ch10
27. Bradley, K., Mallick, R., Andikagumi, H., Hubbard, J., Meilianda, E., Switzer, A., Du, N., Brocard, G., Alfian, D., Benazir, B., Feng, G., Yun, S.H., Majewski, J., Wei, S., Hill, E.M., 2019. Earthquake-triggered 2018 Palu Valley landslides enabled by wet rice cultivation. Nat. Geosci. 12, 935–939. https://doi.org/10.1038/s41561-019-0444-1
28. Watkinson, I.M., Hall, R., 2019. Impact of communal irrigation on the 2018 Palu earthquake-triggered landslides. Nat. Geosci. 12, 940–945. https://doi.org/10.1038/s41561-019-0448-x
29. Mason, H.B., Montgomery, J., Gallant, A.P., Hutabarat, D., Reed, A.N., Wartman, J., Irsyam, M., Simatupang, P.T., Alatas, I.M., Prakoso, W.A., Djarwadi, D., Hanifa, R., Rahardjo, P., Faizal, L., Harnanto, D.S., Kawanda, A., Himawan, A., Yasin, W., 2021. East Palu Valley flowslides induced by the 2018 MW 7.5 Palu-Donggala earthquake. Geomorphology 373. https://doi.org/10.1016/j.geomorph.2020.107482
30. Jaya, A., Nishikawa, O., Jumadil, S., 2019. Distribution and morphology of the surface ruptures of the 2018 Donggala–Palu earthquake, Central Sulawesi, Indonesia. Earth, Planets Sp. 71. https://doi.org/10.1186/s40623-019-1126-3
31. Patria, A., Putra, P.S., 2020. Development of the Palu–Koro Fault in NW Palu Valley, Indonesia. Geosci. Lett. 7. https://doi.org/10.1186/s40562-020-0150-2
32. Wu, D., Ren, Z., Liu, J., Chen, J., Guo, P., Yin, G., Ran, H., Li, C., Yang, X., 2020. Coseismic surface rupture during the 2018 Mw 7.5 Palu earthquake, Sulawesi Island, Indonesia. GSA Bull. https://doi.org/10.1130/b35597.1
33. Natawidjaja, D.H., Daryono, M.R., Prasetya, G., Udrekh, Liu, P.L.F., Hananto, N.D., Kongko, W., Triyoso, W., Puji, A.R., Meilano, I., Gunawan, E., Supendi, P., Pamumpuni, A., Irsyam, M., Faizal, L., Hidayati, S., Sapiie, B., Kusuma, M.A., Tawil, S., 2021. The 2018 Mw7.5 Palu "supershear" earthquake ruptures geological fault's multisegment separated by large bends: Results from integrating field measurements, LiDAR, swath bathymetry and seismic-reflection data. Geophys. J. Int. 224, 985–1002. https://doi.org/10.1093/gji/ggaa498
34. Bao, H., Ampuero, J.P., Meng, L., Fielding, E.J., Liang, C., Milliner, C.W.D., Feng, T., Huang, H., 2019. Early and persistent supershear rupture of the 2018 magnitude 7.5 Palu earthquake. Nat. Geosci. 12, 200–205. https://doi.org/10.1038/s41561-018-0297-z
35. Socquet, A., Hollingsworth, J., Pathier, E., Bouchon, M., 2019. Evidence of supershear during the 2018 magnitude 7.5 Palu earthquake from space geodesy. Nat. Geosci. 12, 192–199. https://doi.org/10.1038/s41561-018-0296-0
36. Fang, J., Xu, C., Wen, Y., Wang, S., Xu, G., Zhao, Y., Yi, L., 2019. The 2018 Mw 7.5 Palu earthquake: A supershear rupture event constrained by InSAR and broadband regional seismograms. Remote Sens. 11. https://doi.org/10.3390/rs11111330
37. Song, X., Zhang, Y., Shan, X., Liu, Y., Gong, W., Qu, C., 2019. Geodetic Observations of the 2018 Mw 7.5 Sulawesi Earthquake and Its Implications for the Kinematics of the Palu Fault. Geophys. Res. Lett. 46, 4212–4220. https://doi.org/10.1029/2019GL082045
38. He, L., Feng, G., Li, Z., Feng, Z., Gao, H., Wu, X., 2019. Source parameters and slip distribution of the 2018 Mw 7.5 Palu, Indonesia earthquake estimated from space-based geodesy. Tectonophysics 772. https://doi.org/10.1016/j.tecto.2019.228216
39. Wang, Y., Feng, W., Chen, K., Samsonov, S., 2019. Source characteristics of the 28 September 2018 Mw 7.4 Palu, Indonesia, earthquake derived from the advanced land observation satellite 2 data. Remote Sens. 11. https://doi.org/10.3390/rs11171999
40. Bacques, G., de Michele, M., Foumelis, M., Raucoules, D., Lemoine, A., Briole, P., 2020. Sentinel optical and SAR data highlights multi-segment faulting during the 2018 Palu-Sulawesi earthquake (Mw 7.5). Sci. Rep. 10. https://doi.org/10.1038/s41598-020-66032-7
41. Li, C., Zhang, G., Shan, X., Zhao, D., Song, X., 2020. Geometric variation in the surface rupture of the 2018 mw7.5 palu earthquake from subpixel optical image correlation. Remote Sens. 12, 1–16. https://doi.org/10.3390/rs12203436
42. Okuwaki, R., Hirano, S., Yagi, Y., Shimizu, K., 2020. Inchworm-like source evolution through a geometrically complex fault fueled persistent supershear rupture during the 2018 Palu Indonesia earthquake. Earth Planet. Sci. Lett. 547. https://doi.org/10.1016/j.epsl.2020.116449

43. Bellier, O., Sébrier, M., Seward, D., Beaudouin, T., Villeneuve, M., Putranto, E., 2006. Fission track and fault kinematics analyses for new insight into the Late Cenozoic tectonic regime changes in West-Central Sulawesi (Indonesia). Tectonophysics 413, 201–220. https://doi.org/10.1016/j.tecto.2005.10.036
44. Socquet, A., Vigny, C., Chamot-Rooke, N., Simons, W., Rangin, C., Ambrosius, B., 2006. India and Sunda plates motion and deformation along their boundary in Myanmar determined by GPS. J. Geophys. Res. Solid Earth 111. https://doi.org/10.1029/2005JB003877
45. Katili, J.A. Past and present geotectonic position of Sulawesi, Indonesia. Tectonophysics 1978, 45, 289–322, doi:10.1016/0040-1951(78)90166-X.
46. Hamilton, W., 1979. Tectonics of the Indonesian region, U.S. Geol. Surv. Prof. Pap. 1078, 345.
47. Silver, E.A., McCaffrey, R., Joyodiwiryo, Y., Stevens, S., 1983a. Ophiolite emplacement by collision between the Sula platform and the Sulawesi island arc, Indonesia. J. Geophys. Res. 88, 9419–9435. https://doi.org/10.1029/JB088iB11p09419
48. Silver, E.A., McCaffrey, R., Smith, R.B., 1983b. Collision, rotation, and the initiation of subduction in the evolution of Sulawesi, Indonesia. J. Geophys. Res. 88, 9407–9418. https://doi.org/10.1029/JB088iB11p09407
49. Hall, R., 1996. Reconstructing Cenozoic SE Asia. Geol. Soc. Spec. Publ. 106, 153–184. https://doi.org/10.1144/GSL.SP.1996.106.01.11
50. Hall, R., 2011. Australia-SE Asia collision: Plate tectonics and crustal flow. Geol. Soc. Spec. Publ. 355, 75–109. https://doi.org/10.1144/SP355.5
51. Watkinson, I.M., Hall, R., 2017. Fault systems of the eastern Indonesian triple junction: Evaluation of Quaternary activity and implications for seismic hazards, in: Geological Society Special Publication. pp. 71–120. https://doi.org/10.1144/SP441.8
52. Bellier, O., Beaudouin, Th, Sebrier, M., Villeneuve, M., Bahar, I., Putranto, E., Pratomo, I., Massault, M. and Seward, D., 1998. Active faulting in Central Sulawesi (Eastern Indonesia). In: The Geodynamics of S and SE Asia (GEODYSSEA) Project Final Report (P. Wilson and G.W. Michel, eds). EC contract CI1*CT93-0337, Scient. Technical Report STR.98±14, 276±312.
53. Bellier, O., Bourles, D.L., Beaudouin, T., Braucher, R., 1999. Cosmic Ray Exposure (CRE) dating in a wet tropical domain: Late Quaternary fan emplacements in central Sulawesi (Indonesia). Terra Nov. 11, 174–180. https://doi.org/10.1046/j.1365-3121.1999.00242.x
54. Bellier, O., Siame, L., Beaudouin, T., Villeneuve, M., Braucher, R., 2001. High slip rate for a low seismicity along the Palu-Koro active fault in Central Sulawesi (Indonesia). Terra Nov. 13, 463–470. https://doi.org/10.1046/j.1365-3121.2001.00382.x
55. Walpersdorf, A.; Vigny, C.; Subarya, C.; Manurung, P. Monitoring of the Palu-Koro Fault (Sulawesi) by GPS. Geophys. Res. Lett. 1998, 25, 2313–2316, doi:10.1029/98GL01799.
56. Stevens, C.; McCaffrey, R.; Bock, Y.; Genrich, J.; Endang; Subarya, C.; Puntodewo, S.S.O.; Fauzi; Vigny, C. Rapid rotations about a vertical axis in a collisional setting revealed by the Palu fault, Sulawesi, Indonesia. Geophys. Res. Lett. 1999, 26, 2677–2680, doi:10.1029/1999GL008344.
57. Vigny, C.; Perfettini, H.; Walpersdorf, A.; Lemoine, A.; Simons, W.; van Loon, D.; Ambrosius, B.; Stevens, C.; McCaffrey, R.; Morgan, P.; et al. Migration of seismicity and earthquake interactions monitored by GPS in SE Asia triple junction: Sulawesi, Indonesia. J. Geophys. Res. Solid Earth 2002, 107, ETG 7-1-ETG 7-11, doi:10.1029/2001jb000377.
58. Daryono, M. Natawidjaja, D.H., Surface rupture of the 1909 event (M7) on Palukoro Fault in tropical forest of Central Sulawesi , Indonesia. Jt. Conv. Yogyakarta 2019, HAGI-IAGI-IAFMI-IATMI 2019.
59. Kaneda, H., Chiba, T., 2019. Stereopaired morphometric protection index red relief image maps (Stereo MPI-RRIMs): Effective visualization of high-resolution digital elevation models for interpreting and mapping small tectonic geomorphic features. Bull. Seismol. Soc. Am. 109, 99–109. https://doi.org/10.1785/0120180166
60. Kaneda, H., Okada, A., 2008. Long-term seismic behavior of a fault involved in a multiple-fault rupture: Insights from tectonic geomorphology along the Neodani Fault, central Japan. Bull. Seismol. Soc. Am. 98, 2170–2190. https://doi.org/10.1785/0120070204
61. Leprince, S., Barbot, S., Ayoub, F., Avouac, J.P., 2007. Automatic and precise orthorectification, coregistration, and subpixel correlation of satellite images, application to ground deformation measurements. IEEE Trans. Geosci. Remote Sens. 45, 1529–1558. https://doi.org/10.1109/TGRS.2006.888937
62. Ayoub, F., Leprince, S., Avouac, J.P., 2009. Co-registration and correlation of aerial photographs for ground deformation measurements. ISPRS J. Photogramm. Remote Sens. 64, 551–560. https://doi.org/10.1016/j.isprsjprs.2009.03.005
63. Avouac, J.P., Ayoub, F., Leprince, S., Konca, O., Helmberger, D. V., 2006. The 2005, Mw 7.6 Kashmir earthquake: Sub-pixel correlation of ASTER images and seismic waveforms analysis. Earth Planet. Sci. Lett. 249, 514–528. https://doi.org/10.1016/j.epsl.2006.06.025
64. Leprince, S., Musé, P., Avouac, J.P., 2008. In-flight CCD distortion calibration for pushbroom satellites based on subpixel correlation. IEEE Trans. Geosci. Remote Sens. 46, 2675–2683. https://doi.org/10.1109/TGRS.2008.918649
65. Bridges, N.T.; Ayoub, F.; Avouac, J.P.; Leprince, S.; Lucas, A.; Mattson, S. Earth-like sand fluxes on Mars. Nature 2012, 485, 339–342, doi:10.1038/nature11022.
66. Hollingsworth, J., Leprince, S., Ayoub, F., Avouac, J.P., 2012. Deformation during the 1975-1984 Krafla rifting crisis, NE Iceland, measured from historical optical imagery. J. Geophys. Res. B Solid Earth 117. https://doi.org/10.1029/2012JB009140

67. Milliner, C.W.D., Dolan, J.F., Hollingsworth, J., Leprince, S., Ayoub, F., Sammis, C.G., 2015. Quantifying near-field and off-fault deformation patterns of the 1992 Mw 7.3 Landers earthquake. Geochemistry, Geophys. Geosystems 16, 1577–1598. https://doi.org/10.1002/2014GC005693
68. Turner, D., Lucieer, A., de Jong, S.M., 2015. Time series analysis of landslide dynamics using an Unmanned Aerial Vehicle (UAV). Remote Sens. 7, 1736–1757. https://doi.org/10.3390/rs70201736
69. Ayoub, F., Leprince, S., Keene, L., 2009. User's Guide to COSI-CORR Co-registration of Optically Sensed Images and Correlation. Book 1–38.
70. Meygret, A.; Baillarin, S.; Gascon, F.; Hillairet, E.; Dechoz, C.; Lacherade, S.; Martimort, P.; Spoto, F.; Henry, P.; Duca, R. SENTINEL-2 image quality and level 1 processing. In Proceedings of the Earth Observing Systems XIV; SPIE, 2009; Vol. 7452, p. 74520D.
71. Chen, W.S., Yang, C.Y., Chen, S.T., Huang, Y.C., 2020. New insights into Holocene marine terrace development caused by seismic and aseismic faulting in the Coastal Range, eastern Taiwan. Quat. Sci. Rev. 240. https://doi.org/10.1016/j.quascirev.2020.106369
72. Broecker, W.S., Andree, M., Wolfli, W., Oeschger, H., Bonani, G., Kennett, J., Peteet, D., 1988. The chronology of the last Deglaciation: Implications to the cause of the Younger Dryas Event. Paleoceanography 3, 1–19. https://doi.org/10.1029/PA003i001p00001
73. Cowgill, E., 2007. Impact of riser reconstructions on estimation of secular variation in rates of strike-slip faulting: Revisiting the Cherchen River site along the Altyn Tagh Fault, NW China. Earth Planet. Sci. Lett. 254, 239–255. https://doi.org/10.1016/j.epsl.2006.09.015
74. Tsuji, T., Ishibashi, J., Ishitsuka, K., Kamata, R., 2017. Horizontal sliding of kilometre-scale hot spring area during the 2016 Kumamoto earthquake. Sci. Rep. 7. https://doi.org/10.1038/srep42947
75. Fujiwara, S., Morishita, Y., Nakano, T., Kobayashi, T., Yarai, H., 2017. Non-tectonic liquefaction-induced large surface displacements in the Aso Valley, Japan, caused by the 2016 Kumamoto earthquake, revealed by ALOS-2 SAR. Earth Planet. Sci. Lett. 474, 457–465. https://doi.org/10.1016/j.epsl.2017.07.001
76. Lin, A., Chen, P., Sado, K., 2018. Recurrent large earthquakes related with an active fault-volcano system, southwest Japan. Sci. Rep. 8. https://doi.org/10.1038/s41598-018-32140-8
77. Ben-Avraham, Z., Almagor, G., Garfunkel, Z., 1979. Sediments and structure of the Gulf of Elat (Aqaba)-Northern Red Sea. Sediment. Geol. 23, 239–267. https://doi.org/10.1016/0037-0738(79)90016-2
78. Ben-Avraham, Z., 1985. Structural framework of the Gulf of Elat (Aqaba), northern Red Sea. J. Geophys. Res. 90, 703–726. https://doi.org/10.1029/JB090iB01p00703
79. Garfunkel, Z., Ben-Avraham, Z., 1996. The structure of the Dead Sea basin. Tectonophysics 266, 155–176. https://doi.org/10.1016/S0040-1951(96)00188-6
80. Ehrhardt, A., Hübscher, C., Ben-Avraham, Z., Gajewski, D., 2005. Seismic study of pull-apart-induced sedimentation and deformation in the Northern Gulf of Aqaba (Elat). Tectonophysics 396, 59–79. https://doi.org/10.1016/j.tecto.2004.10.011
81. Earthquake Research Committee, Headquarters for Earthquake Research Promotion, 2015. Long-term Evaluation of Seismic Risk in the Itoigawa-Shizuoka Tectonic Line Fault Zone. Second edition. p14. https://www.jishin.go.jp/main/chousa/katsudansou_pdf/41_42_44_itoigawa-shizuoka_2.pdf (in Japanese)
82. Fujimori, T., 1991. Active faults in the Suwa Basin, and its evolution as a pull-apart basin on the Itoigawa-Shizuoka Tectonic Line, central Japan. Geogr. Rev. Jpn Ser. A 64, 665–696. https://doi.org/10.4157/grj1984a.64.10_665 (in Japanese with English abstract)
83. Fujimori, T., Ota, Y., 1992. Strip map of active faults on the Suwa Basin, Central Japan, 1992. . Act. Fault Res. 1992, 27–39. https://doi.org/10.11462/afr1985.1992.10_27 (in Japanese with English abstract)
84. Imaizumi, T., Togo, M., Sawa, H., Ikeda, Y., Matsuta, N., 1998. 1:25,000 Active Fault Map, Itoigawa-Shizuoka Tectonic Line and its vicinity "Suwa." Geospatial Information Authority of Japan, 56, D1-No.368 (in Japanese)
85. Sawa, H., Togo, M., Imaizumi, T., Ikeda, Y., 1997. 1:25,000 Active Fault Map, Itoigawa-Shizuoka Tectonic Line and its vicinity "Chino." Geospatial Information Authority of Japan, 46, D1-No.355 (in Japanese)
86. Sugito, N., Sawa, H., Taniguchi, K., Sato, Y., Watanabe, M., Suzuki, Y., 2019. Evolution of Riedel-shear pop-up structures during cumulative strike-slip faulting: A case study in the Misayama-Godo area, Fujimi Town, central Japan. Geomorphology 327, 446–455. https://doi.org/10.1016/j.geomorph.2018.11.026
87. Miyakoshi, K., Ueta, K., Hataya, R., Abe, S., Miura, D., Hamada, Y, Aoyagi, Y., Inoue, D., 2004, A proposal of surveying and evaluating system of active faults for earthquake assessment. Denryoku Chuo Kenkyusho Hokoku, (U46), 1-8,1-189. https://inis.iaea.org/search/search.aspx?orig_q=RN:36014835